REPORT DOCUMENTATION PAGE

AFRL-SR-BL-TR-98-

0630

1. AGENCY USE ONLY (Leave blank)	2. REPORT DATE	3. REPORT TYPE AND DATES COVERED
		Annual Prog. Rpt., 15Nov97 to 15Aug98

4. TITLE AND SUBTITLE
(U) Fundamentals of Soot Formation in Gas Turbine Combustors

5. FUNDING NUMBERS
PE - 61102F
PR - 2308
SA - BS
C - F49620-98-C-0008

6. AUTHOR(S)
Meredith B. Colket, III, Robert J. Hall, David S. Liscinsky and Mitchell D. Smooke

7. PERFORMING ORGANIZATION NAME(S) AND ADDRESS(ES)
United Technologies Research Center
411 Silver Lane
East Hartford, CT 96108

8. PERFORMING ORGANIZATION REPORT NUMBER
UTRC98-5.100.0016-1

9. SPONSORING / MONITORING AGENCY NAME(S) AND ADDRESS(ES)
AFOSR/NA
110 Duncan Avenue, Suite B115
Bolling AFB DC 20332-0001

10. SPONSORING / MONITORING AGENCY REPORT NUMBER

11. SUPPLEMENTARY NOTES

12a. DISTRIBUTION / AVAILABILITY STATEMENT
Approved for public release; distribution is unlimited

12b. DISTRIBUTION CODE

13. ABSTRACT (Maximum 200 words)

An experimental facility for studying soot formation in high temperature, fuel-rich, laminar, premixed flames has been constructed. Diagnostics included laser absorption, thermocouple particle densitometry, and thermophoretic soot sampling with analysis by transmission electron microscopy. Single particles with diameters as small as 3-5 nanometers were observed. Larger particles (20-25 nanometers) agglomerated to form large clusters. A coflow, axisymmetric, laminar ethylene diffusion flame has been studied, both experimentally and computationally. A lifted flame has been selected to eliminate possible uncertainties caused by the burner lip. A two-dimensional, detailed soot growth model in which the equations for particle production are coupled to the flow and gaseous species conservation equations has been used to investigate soot production in the flame. Detailed transport and finite rate chemistry in the gas phase was coupled with the particle aerosol equations in the sectional representation. In comparison to measured data obtained using intrusive and non-intrusive diagnostics, the model predicted temperature, flame height, and major species very well. Peak benzene concentrations and soot volume fraction were predicted to within 20% of the experimental value. The predicted distribution of benzene was excellent, but the soot was underpredicted along the centerline. This deficit was attributed to limitations in the PAH growth model. Oxidation of particulates was dominated by reactions with hydroxyl radical at superequilibrium levels. Radiation losses significantly effected predicted temperatures.

14. SUBJECT TERMS	15. NUMBER OF PAGES
coflow, laminar, diffusion ethylene flames, soot formation, modeling, particle size, effects of radiation, agglomeration premixed flames	94
	16. PRICE CODE

17. SECURITY CLASSIFICATION OF REPORT	18. SECURITY CLASSIFICATION OF THIS PAGE	19. SECURITY CLASSIFICATION OF ABSTRACT	20. LIMITATION OF ABSTRACT
Unclassified	Unclassified	Unclassified	UL

FUNDAMENTALS OF SOOT FORMATION IN GAS TURBINE COMBUSTORS

Annual Progress Report
November 15, 1997 to August 15, 1998

AFOSR Contract F49620-98-C-0008

Principal Investigators:
Meredith B. Colket and Robert J. Hall

Co-Investigator:
David Liscinsky

United Technologies Research Center
Silver Lane, E. Hartford, CT 06108

Prepared with assistance from
M. D. Smooke
Yale University

UTRC Report No. UTRC98-5.100.0016-1

J. M. Tishkoff
Program Manager
August 31, 1998

FUNDADMENTALS OF SOOT FORMATION IN GAS TURBINE COMBUSTORS

Annual Progress Report

Table of Contents

FUNDAMENTALS OF SOOT FORMATION IN GAS TURBINE COMBUSTORS

Annual Progress Report
November 15, 1997 to August 15, 1998

AFOSR Contract F49620-98-C-0008

I. Objectives

The overall objectives of this work are to obtain necessary fundamental data and to enhance and then validate modeling procedures in order to support modeling of soot production in practical gas turbine combustors. Several focused tasks of this effort include (1) extending measurements of surface growth rate constants to high temperatures, characteristic of rich zones in advanced combustors; (2) modeling of steady, laminar diffusion flames with different fuels to assist in validating the models; (3) advancing the modeling capabilities for describing known physical processes involved in soot production, including carbonization, ageing, and aggregate formation to enable more reliable extrapolation of existing models; and (4) modeling of sooting, transient flames to offer some physical understanding of processes controlling soot formation and destruction in turbulent, diffusion flames.

II. Status of Effort

The contract initiated at the end of last year. One major success was a collaborative effort with experimentalists at Yale, resolving a problem in modeling flame heights and writing a paper on modeling a coflow laminar, ethylene flame which was accepted and presented at the 27th International Combustion Symposium (see Appendix A). This work has been useful in identifying strengths and weaknesses in both experiments and in our model. A new laboratory facility for studying soot formation in atmospheric pressure, premixed flames has been constructed. Appropriate diagnostic tools have been acquired and tested in preparation for measuring surface growth rates of soot particulates at high temperatures. New procedures are being developed to treat agglomerate structures in flames. In addition, refinements to a previous manuscript have been completed and it has been accepted for publication (Appendix B).

III. Accomplishments/New Findings

III. A. Measurements of Surface Growth Rates at High Temperatures

An important parameter for the prediction of soot production is the surface growth rate. Virtually all reliable measurements of this parameter have been obtained over the temperature range of 1500-1950K. Many authors simulate this rate using a rate constant which increases exponentially with temperature (Arrhenius formulation). This assumption is acceptable under standard conditions since soot formation usually occurs in diffusion flames at temperatures below 1800K. Ref 1 and 2 have separately developed temperature-dependent expressions showing a substantial fall-off in the net rate constant for surface growth above about 1850K. These formulations were in part developed based on limited data at elevated temperatures (see Ref 3). Reliable data at temperatures above 2000K is very limited and hence extrapolation of this fall-off trend is highly uncertain. This problem is a concern since for advanced, high performance gas turbine combustors the 'sooting' rich zone will be at temperatures well in excess of 2000K. This problem is depicted in Figure 1 in which equilibrium temperatures for several different conditions are plotted. The temperatures computed with the heated ethylene fuel and high air preheat can be taken as advanced combustor conditions. Since most data is obtained for the lower temperature zone, there is an obvious concern in extrapolating existing models to the conditions of the advanced combustors.

Figure 1

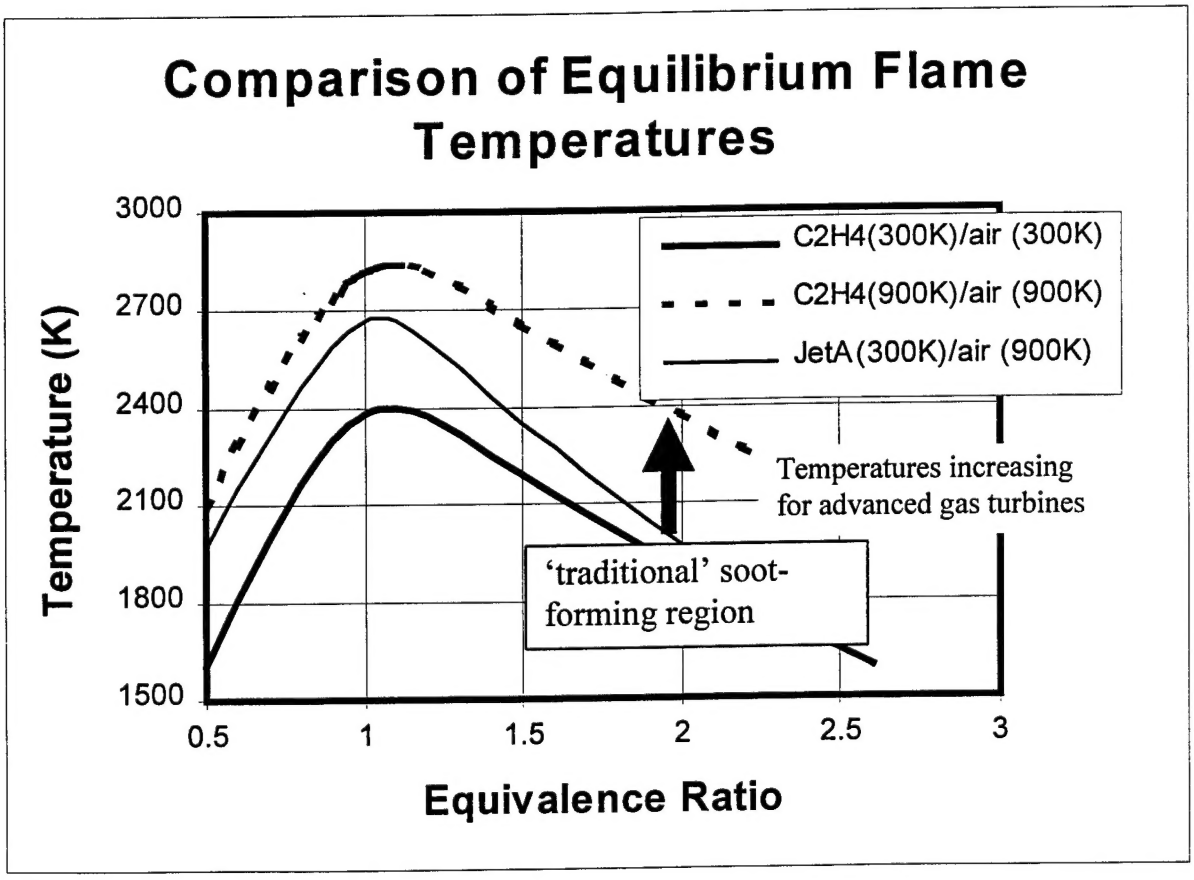

To provide the needed data, a series of fuel-rich, laminar premixed flames are being examined, analogous to several previous studies (see for example, Ref. 4-5). Soot evolution in ethylene/oxygen/argon flames with C/O ratios from 0.56 to 0.92 have been characterized using laser extinction, thermocouple particle densitometry (TPD), and thermophoretic sampling followed by transmission electron microscopy (TEM).

Initial measurements of soot volume fraction using TPD were in good agreement with those made using laser extinction. The measurements were made on a custom hastalloy burner containing 513 x 1.2mm diameter holes spaced 2.0mm o.c. (28% open area) which is surrounded by a co-flow. Concern over the uniformity and ultimate flame holding ability at future flow conditions of this burner design prompted a redesign to a sintered metal surface burner. Results from the new burner will be used to finalize our implementation of the TPD technique which depends on proper analysis of the soot deposition stages of the thermocouple junction.

Rapid insertion and withdrawal of 3mm diameter carbon-coated TEM grids accomplished thermophoretic sampling in the flame. Subsequent inspection of the deposits using TEM indicated the presence of individual (as small as 5 nm diameter) and agglomerated particles. The agglomerate size increased with downstream distance while (consistent with prior work) the primary particle size in the agglomerates remained about 20nm. A computer controlled sampling system is nearing completion and further refinement of the TEM analysis is required.

III. B. Modeling of Soot Formation in Diffusion Flames

In addition to work in modeling opposed jet diffusion flames (see Ref. 6-7), significant accomplishments in the modeling of a coflow, laminar diffusion flame model have been achieved. Most studies in which detailed chemical kinetics are coupled with detailed soot models have been focused on one-dimensional problems. Ref. 8 and 9 have modeled laminar jet diffusion flames using monodisperse soot formation models with skeletal reaction mechanisms. In this program, we have incorporated the sectional soot formation and radiation models developed in Ref. 1 and 6 into the laminar, axisymmetric, diffusion flame code (see Ref. 10) for a cylindrical fuel stream surrounded by a coflowing oxidizer jet. This recent work is described in detail in Ref. 11 (Appendix B) for an attached methane flame and in Ref. 12 (Appendix A) for a diluted, lifted ethylene flame. For methane, a modified GRIMech 2.11, with all NO related reactions deleted and some benzene formation and destructions steps added, was used for the computations. The ethylene mechanism was derived from GRIMech, based on comparisons to PSR data and ignition delay times. We have collaborated with colleagues at Yale who have been investigating these flames using a variety of experimental techniques (thermocouples, TPD, quartz probes with on-line mass spectrometry and, in the case of the ethylene study, planar laser imaging using Rayleigh scattering and laser-induced incandescence).

For the attached methane flame, qualitative agreements were good, but several quantitative differences between the model and experiment were apparent. Most of these were attributable to an inability to model accurately the bulk flow features of the flame (particularly flame height was over predicted and peak flame temperatures were under predicted. Given these important differences, the agreement of species concentrations and soot profiles were quite good. However, quantitative comparisons between the measured and predicted soot profiles could not be made (predictions were about a factor of four low). Predicted distributions of particle size as a function of radius is shown in Fig. 2 at a height of 3 cm (approximately one cm below the height at which the peak centerline value is obtained). These distributions can be shown to be representative of the two soot producing regions of the flame. One along the wings (just inside of the flame front) where peak volume fractions are attained and the other along the centerline where much slower growth and particle sizes are observed.

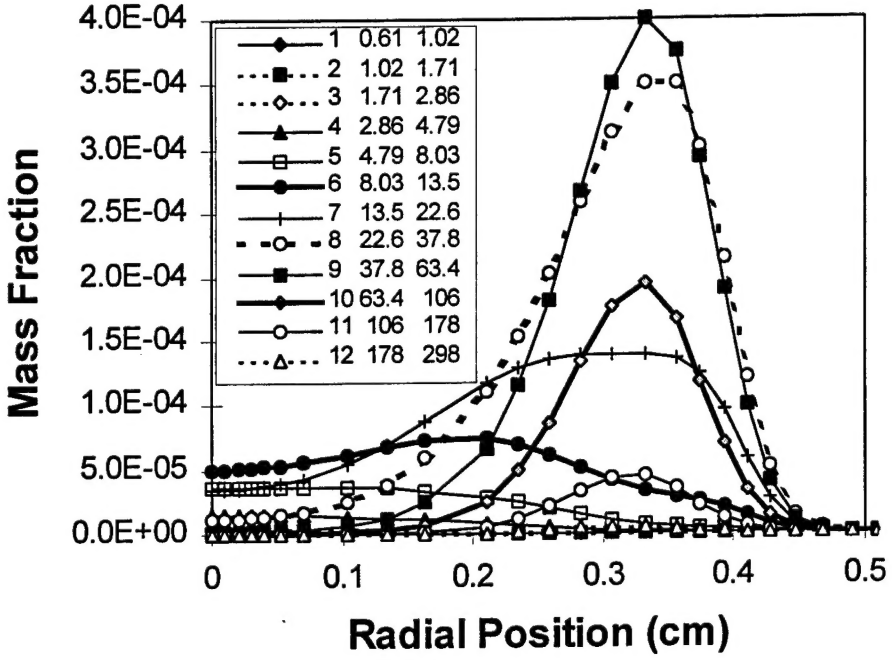

Figure 2. Contributions of various soot mass classes to the total soot volume fraction as a function of radius at a height of 3 cm. Labels for the mass classes include the minimum and maximum diameters (nm).

The diluted lifted ethylene flame was selected in order to avoid possible complications of interactions between the burner lip and the flame, a possible source of the above discrepancies. In addition, optical diagnostics were included to add additional information to help resolve any differences between the model and physical probing of the flame. Overall, the agreements between the model and the experiments were extremely good for many features of the flame. Between the three 'solutions' for the ethylene flame (one model and two experiments), usually at least two of the methods

agreed well (both spatial distributions and quantitative values). A comparison of the gas sampling and model predictions for benzene is shown in Fig. 4 of Appendix A, with identical scales for both contour plots. Very good qualitative and quantitative agreement is obtained. A limitation in the soot model can be illustrated by examining Fig. 3a, b, and c, which compare contour plots of total soot volume fraction for the model and the two experimental methods. While the maximum values of soot volume are reproduced well, the predicted soot profiles peak in the wing tips, while both experimental methods (TPD and LII) peak along the centerline. A preliminary analysis of this failure in the model is its inability to reproduce accurately the processes of early PAH formation occurring along the centerline of the burner. Additional work in this area is proceeding as are initial efforts to model the 'Santoro' ethylene diffusion flame.

Figure 3. Comparison of predicted and measured soot volume fractions

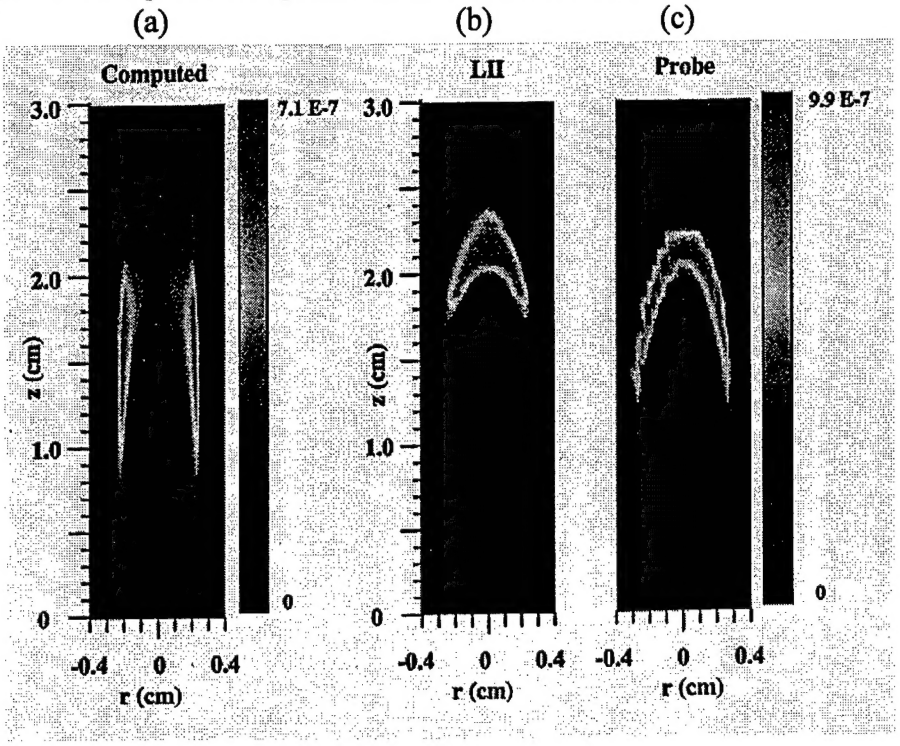

III. C . Modeling the Growth and Oxidation of Soot Aggregates

In modeling the growth of soot particles, it has been conventional to assume, for simplicity, that the particles consist of isolated spheroids, which undergo surface growth and oxidation, and coalesce with one another on impact. The experimental evidence, however, is that while the coalescing spheroid picture is accurate for very small (young) particles, older soot particles tend to consist of chainlike aggregates of primary spheroids which fuse together on impact but do not coalesce. The sectional aerosol dynamics representation that has been used to model the growth of spheroids is being adapted to model aggregates, as well.

The algorithm being adapted for use in soot kinetics has a provision for a "discrete" size range of precursor particles whose masses are multiples of some monomer growth species. The discrete size range is joined to an isolated spheroid size range whose boundaries vary linearly on a logarithmic scale; these "liquid" particles are assumed to coalesce on collision. Beyond an arbitrarily determined size, particles are assumed to fuse with one another, leading to aggregate formation. The conventional spheroid sectional analysis tracks the total mass density within set sectional boundaries; the extended sectional analysis tracks not only the mass density, but also the number of primary particles within a section. Aggregate-aggregate collisons leading to larger aggregates are prescribed at rates based on an assumed fractal dimension for the clusters.

III. D. References

1. M. Colket and R. Hall, Proceedings of the International Workshop on Mechanism and Models of Soot Formation (H. Bockhorn, Ed.), Springer-Verlag, Heidelberg, (1994).
2. P. Markatou, H. Wang, and M. Frenklach, C&F, **93**, 467 (1993).
3. H. Bockhorn, F. Fetting, and H. Wenz, Ber. Bunsenges. Phys. Chem., **87**, 1067 (1983).
4. S. Harris, A. Weiner and R. Blint, C&F 72, 91 (1988). And references contained therein.
5. P. Sunderland and G. Faeth, C&F **105**, 132 (1996).
6. R. Hall, M. Smooke, and M. Colket, in Physical and Chemical Aspects of Combustion, Combustion Science and Technology Book Series (1997).
7. M. Smooke, R. Hall, and M. Colket, "Application of Continuation Methods to Soot Formation in Diffusion Flames," submitted for publication, (1998).
8. C. Kaplan, C. Shaddix and K. Smyth, C&F **106**, 392 (1996).
9. I. Kennedy, D. Rapp, R. Santoro, and C. Yam, C&F **107**, 368 (1996).
10. M. Smooke, Y. Xu, R. Zurn, P. Lin, J. Frank, and M. Long, Twenty-Fourth Symposium (International) on Combustion, The Combustion Institute, Pittsburgh, p. 813, (1992).
11. M. Smooke, C. McEnally, L. Pfefferle, R. Hall, and M. Colket, "Computational and Experimental Study of Soot Formation in a Coflow, Laminar Diffusion Flame", accepted for publication in Combustion and Flame, 1998.
12. C. McEnally, A. Schaffer, M. Long, L. Pfefferle, M. Smooke, M. Colket, and R. Hall, "Computational and Experimental Study of Soot Formation in a Coflow, Laminar Ethylene Diffusion Flame", Oral presentation at the 27th International Symposium on Combustion, Boulder, CO, 1998.

IV. Personnel Supported

Key personnel contributing to this project are:
Dr. Meredith B. Colket, III of United Technologies Research Center
Mr. Robert J. Hall of United Technologies Research Center
Mr. David S. Liscinsky of United Technologies Research Center
Professor Mitchell D. Smooke of Yale University

V. Publications

C. S. McEnally, A. M. Schaffer, M. B. Long, L. D. Pfefferle, M. D. Smooke, M. B. Colket, and R. J. Hall, "Computational and Experimental Study of Soot Formation in a Coflow, Laminar Ethylene Diffusion Flame," To be published in the Twenty-Seventh Symposium (International) on Combustion (1999) (see Appendix A.)

M. D. Smooke, C. S. McEnally, L. D. Pfefferle, R. J. Hall, and M. B. Colket, "Computational and Experimental Study of Soot Formation in a Coflow, Laminar Diffusion Flame," To be published in Combustion and Flame. (1998) (see Appendix B.)

VI. Interactions/Transitions

VI. A. Meetings

On October 27-29, 1997, M. Colket, D. Liscinsky, R. Hall and M. D. Smooke attended the Fall Technical Meeting of the Eastern States Section of the Combustion Institute at Hartford, CT. A paper entitled "Interpretations of a Computational Study of Soot Formation Coflow, Laminar Diffusion Flame" by M. Smooke, R. Hall, and M. Colket was presented.

On March 29-April 1, 1998, M. Colket attended the 20th Annual Combustion Research Conference of the US. DOE, Basic Energy Sciences, Dallas, TX. This meeting was held in conjunction with the American Chemical Society National Meeting.

On April 21^{st,} 1998, M. Colket went to NASA LeRC and led discussions on particulate measurements and soot modeling.

On August 2-7, 1998, M. Colket, R. Hall, and M. Smooke attended the 27th International Symposium on Combustion in Boulder, CO. A paper entitled "Computational and Experimental Study of Soot Formation in a Coflow, Laminar Ethylene Diffusion Flame" was presented. In addition, a (related, but separately supported) poster paper entitled "Computational and Experimental Study of C_1 to C_6 Hydrocarbons in a Steady, Axisymmetric Flame" was presented.

VI. B. Advisory Functions

None

VI. C. Transitions

In 1997 and 1998, M. Colket refined software for rapidly calculating equilibrium temperatures and NOx formation and transferred it to Dr. Saadat Syed ((561)796-3560) of Pratt and Whitney for imbedding into a CFD design code.

VII. Record of Inventions

There were no inventions during this reporting period. (DD Form 882, Interim Patent Report to be submitted under separate cover)

VIII. Honors/Awards

M. Colket, as a member of a CFD development team, has been nominated and is a finalist for the 1998 Pratt and Whitney Leadership Award.

Principal Investigator Annual Data Collection (PIADC) Survey Form

NOTE: If there is insufficient space on this survey to meet your data submissions, please submit additional data in the same format as identified below.

PI DATA

Name (Last, First, MI): Colket, Meredith B. III

Institution: United Technologies Research Center

Contract/Grant No: F49620-98-C-0008

AFOSR USE ONLY
Project/Subarea
_____/____

NX _____

FY _____

NUMBER OF CONTRACT/GRANT CO-INVESTIGATORS

Faculty 1 Post Doctorates _____ Graduate Students _____ Other 2

PUBLICATIONS RELATED TO AFOREMENTIONED CONTRACT/GRANT

NOTE: List names in the following format: Last Name, First Name, MI

Include: Articles in peer reviewed publications, journals, book chapters, and editorships of books.

Do Not Include: Unreviewed proceedings and reports, abstracts, "Scientific American" type articles, or articles that are not primary reports of new data, and articles submitted or accepted for publication, but with a publication date outside the stated time frame

Name of Journal, Book, etc: Combustion and Flame

Title of Article: Computational and Experimental Study of Soot Formation in a Coflow, Laminar Diffusion Flame

Author(s): M. Smooke, C. McEnally, L. Pfefferle, R. Hall and M. Colket

Publisher (if applicable): Elsevier

Volume: _____ Page(s): _____ Month Published: _____ Year Published: 1998

Name of Journal, Book, etc: Twenty-Seventh Symposium (Int'l) on Combustion

Title of Article: Computational and Experimental Study of Soot Formation in a Coflow, Laminar Ethylene Diffusion Flame

Author(s): M. Smooke, E. McEnally, L. Pfefferle, A. Schaffer, M. Long, M. Colket, R. Hall

Publisher (if applicable): The Combustion Institute

Volume _____ Page(s) _____ Month Published: _____ Year Published: 1998

HONORS/AWARDS RECEIVED DURING CONTRACT/GRANT LIFETIME

Include: All honors and awards received during the lifetime of the contract or grant, and any life achievement honors such as (Nobel prize, honorary doctorates, and society fellowships) prior to this contract or grant.

Do Not Include: Honors and awards unrelated to the scientific field covered by the contract/grant.

Honor/Award: Pratt & Whitney Leadership Award Year Received: 1998 (Finalist)

Honor/Award Recipient(s): M. Colket (with CFD development team)

Awarding Organization: Pratt & Whitney

Appendix A
Computational and Experimental Study of Soot Formation in a Coflow, Laminar Ethylene Diffusion Flame

COMPUTATIONAL AND EXPERIMENTAL STUDY OF SOOT FORMATION IN A COFLOW, LAMINAR DIFFUSION FLAME

M. D. Smooke, C. S. McEnally, L. D. Pfefferle
Yale Center for Combustion Studies
Yale University, New Haven, CT 06520
and
R. J. Hall and M. B. Colket
United Technologies Research Center
E. Hartford, CT 06108

Abstract

A detailed soot growth model in which the equations for particle production have been coupled to the flow and gaseous species conservation equations has been developed for an axisymmetric, laminar, coflow diffusion flame. Results from the model have been compared to experimental data for a confined methane-air flame. The two-dimensional system couples detailed transport and finite rate chemistry in the gas phase with the aerosol equations in the sectional representation. The formulation includes detailed treatment of the transport, inception, surface growth, oxidation, and coalescence of soot particulates. Effects of thermal radiation and particle scrubbing of gas phase growth and oxidation species are also included. Predictions and measurements of temperature, soot volume fractions and selected species are compared over a range of heights and as a function of radius. Flame heights are somewhat overpredicted and local temperatures and volume fractions are underpredicted. We believe the inability to reproduce accurately bulk flame parameters directly inhibits the ability to predict soot volume fractions and these differences are likely a result of uncertainties in the experimental inlet conditions. Predictions of the distributions of particle sizes indicate the existence of (relatively) low molecular weight species along the centerline of the burner and trace amounts of the particles which escape from the flame, unoxidized. Oxidation of particulates is dominated by reactions with hydroxyl radicals which attain levels approximately ten times higher than calculated equilibrium levels. Gas cooling effects due to radiative loss are shown to have a very significant effect on predicted soot concentrations.

COMPUTATIONAL AND EXPERIMENTAL STUDY OF SOOT FORMATION IN A COFLOW, LAMINAR DIFFUSION FLAME

1. Introduction

In the last few years, we have witnessed a shift in combustion research. The push for higher combustion efficiency in propulsion applications that dominated much of research in the past few decades is gradually being replaced by a drive towards *cleaner* combustion. This is a direct result of environmental consciousness and it has been translated into stricter air quality legislation. Although it originated as a reaction to regulatory pressure, research in the area of pollutant formation and control will become economically indispensable to the export of combustion-related technologies and products worldwide. In particular, as emissions legislation becomes more restrictive, a detailed understanding of soot formation and unburned hydrocarbons in flames will be critical for the design of pollutant abatement strategies and for the preservation of the competitiveness of combustion related industries.

Modeling soot formation in practical combustion systems is an extremely challenging problem. Reacting flow problems for simple fuels such as methane can require the solution of more than 50 chemical species in addition to the temperature *and* the fluid dynamic variables. The inclusion of soot inception, growth and oxidation processes in these models greatly increases the level of complexity of the problem. In fact, due to the number of dependent unknowns and the resolution with which reaction fronts need to be resolved, *gas phase* combustion calculations with detailed chemistry have only recently moved from one- to two- and some three-dimensional systems. The increased effort with which multidimensional combustion phenomena have been studied numerically is attributable in part to advances in the development of computational algorithms, and in part to higher speed/larger memory workstations. This combination has enabled the combustion scientist to investigate chemically reacting systems that were computationally infeasible only a few years ago. Nevertheless, the investigation of soot formation with detailed chemistry in a generic multidimensional configuration is still beyond our current computational ability. The laminar diffusion flame, however, provides a natural environment in which one can investigate the interaction of soot formation with detailed gas-phase chemistry in a multidimensional system.

Most studies using detailed chemical kinetics and coupled models of soot production and oxidation have focused on one-dimensional geometries. A few recent studies [Kaplan *et al.*, 1996, Kennedy *et al.*, 1996] have focused on jet diffusion flames, using simplified, monodisperse, soot formation models with skeletal kinetic mechanisms. In this paper we modify the sectional soot formation model developed in Colket and Hall (1994) and Hall *et al.* (1997) for incorporation into a laminar, axisymmetric, diffusion flame in which a cylin-

drical fuel stream is surrounded by a coflowing oxidizer jet. Computationally, we employ a velocity-vorticity model (Ern *et al.*, 1995) in which the governing conservation equations are solved with detailed transport and finite rate chemistry submodels to predict the temperature, species mass fractions and velocity fields as functions of the two independent coordinates. Appropriate sectional equations are included for describing the different soot particle size classes with a convective, diffusive and chemical production balance. These equations, along with surface growth, oxidation and radiation (from both gas and particulate species) are fully integrated with the governing equations. A discrete solution is obtained on a two-dimensional grid by employing Newton's method with adaptive mesh refinement. In many models diffusion in the axial direction is neglected: here, we consider the fully elliptic problem. Experimentally, we utilize thermocouple particle densitometry and mass spectrometry to obtain profiles of the soot volume fraction and the species concentrations at various heights in the flame (McEnally and Pfefferle, 1997).

2. Problem Formulation

While the ultimate goal in combustion modeling is the solution of three-dimensional turbulent reacting flows with finite rate chemistry, there are still important less complex systems that can be analyzed in detail with current computational resources. The axisymmetric, laminar, diffusion flame is one such configuration (Smooke *et al.*, 1990, 1992, 1996; Xu *et al.*, 1993; Ern *et al.*, 1995). Diffusion flames are typical of most practical combustion devices. The ability to predict the coupled effects of complex transport phenomena with detailed chemical kinetics even in laminar systems is useful in the modeling of turbulent reacting flows and in understanding the processes by which pollutants are formed.

2.1 Soot Modeling

Soot kinetics are modeled as coalescing, solid carbon spheroids undergoing surface growth in the free molecule limit. The particle mass range of interest is divided into sections (Gelbard and Seinfeld, 1980), and an equation is written for each section including coalescence, surface growth, and oxidation. In the sectional representation, the sectional mass boundaries vary linearly on a logarithmic scale. Sectional analysis makes it possible to obtain the particle size distribution without apriori assumptions about the form of the distribution. For the first bin, an inception source term is included. The incorporation of these equations into a transport/conservation equation for each section includes both thermophoresis and an effective bin diffusion rate. In the gas species conservation equations, provision is made for complex chemistry; additional source terms are included to account for scrubbing or generation of gaseous species arising from the particle growth and oxidation processes. The gas and soot are additionally coupled through non-adiabatic radiative loss from both the gas and the soot in the optically-thin approximation. For one atmosphere calculations, the sectional coefficients for transport, coalescence and surface

processes are calculated in the free molecule limit (Gelbard and Seinfeld, 1980), with surface growth and oxidation proportional to particle surface area. In the free molecule limit, the dependencies of the sectional coefficients of the particle mass in its surrounding gas medium are factored in such a way that they only have to be evaluated once. Oxidation of soot by O_2 and OH is treated as described in (Hall *et al.*, 1997). The inception model employed here is based on an estimate of the formation rate of two- and three-ringed aromatic species, and is a function of local acetylene, benzene, phenyl and molecular hydrogen concentrations. Assuming steady-state values of intermediates, and also that $H_2 >> C_2H_2$, the rate of production of the polyaromatic species can be estimated to be (Hall *et al.*, 1997)

$$\frac{d[C_{10}\dot{H}_7]}{dt} = 10^{11.88} e^{(-4378/T)} \frac{[C_2H_2]^2}{[H_2]} [C_6\dot{H}_5] \text{ cc/mole/sec}, \tag{2.1}$$

and

$$\frac{d[C_{14}H_{10}]}{dt} = 10^{12.50} e^{(-6390/T)} \frac{[C_2H_2]}{[H_2]} [C_6H_6][C_6\dot{H}_5] \text{ cc/mole/sec}, \tag{2.2}$$

where the gas phase concentrations and temperatures are evaluated at local conditions. With the further assumptions that inception is limited by the formation of polyaromatics and oxidation/decomposition of such species can be neglected, the inception rate, S_i, in grams/cc/sec, was initially assigned to

$$S_i = 127 \times \frac{d[C_{10}\dot{H}_7]}{dt} + 178 \times \frac{d[C_{14}H_{10}]}{dt}, \tag{2.3}$$

where the constants (molecular weights) are provided to convert from molar to mass units. The second term in equation 2.3 plays a negligible role in methane-air diffusion flames but has been included here for generality. The contributions from both inception processes are incorporated in the first sectional bin, whose lower mass boundary is set equal to the mass of the smallest inception species (See Section 5).

This inception model contrasts with those utilized by Frenklach and coworkers, see Markatou, et al., (1993) and references contained therein. Originally, such models included detailed chemical kinetics to describe the formation of very large molecular weight species. Their inception model has subsequently been modified to include the dimerization of much smaller PAH species, such as pyrene ($C_{16}H_{10}$). Our use of smaller species for inception likely overestimates the initial rates of inception, but then also overestimates rates of coalescence which reduces surface area and surface growth. While these effects are not counterbalanced, the uncertainties in PAH formation models and their role in soot nucleation do not yet justify the use of the more detailed approach.

The surface growth rate is nominally that of Harris and Weiner (1983), who report a rate proportional to acetylene concentration near 1650 K. We have imposed a 31.8 kcal/mole activation energy as suggested by Hura and Glassman (1988), and have empirically multiplied the surface growth Arrhenius A-factor by a factor of two. The enhancement by a factor of two brings the Harris and Weiner rate, determined from studies on premixed ethylene flames, into better agreement with results obtained in diffusion flames (Axelbaum *et al.*, 1988, Kennedy *et al.*, 1990, Sunderland and Faeth, 1996), where somewhat larger surface growth rates have been measured.

It is not suggested that the soot growth model used here represents a universal solution to the problem of soot formation because comparisons with soot growth from other fuels have not been performed. The possibility of aging of the surface growth rate is not accounted for here, nor is aggregate formation. These effects should be included in future modeling efforts. Fundamental questions remain regarding inception, temperature dependence of surface growth and precise dependence of surface growth on gas phase species concentrations. Whether soot growth rates derived from premixed and opposed jet studies are self-consistent is still an open issue as well.

The number of soot sections required for convergence of soot size/density parameters must be examined in each problem, although evidence points to the relative magnitudes of surface growth and inception as determining this number. When the contribution of inception to total volume fraction is significant, although not necessarily dominating, the number of sections required can be very small (Hall *et al.*, 1997), with larger numbers necessary when the contribution of surface growth to volume fraction becomes very much larger than that from inception.

2.2 Governing Equations

If we combine the gas-phase diffusion flame model which employs a velocity-vorticity formulation (Ern *et al.*, 1995) with the sectional approach presented in Hall *et al.* (1997), the coupled set of governing partial differential equations can be written in the form

Radial Velocity

$$\frac{\partial^2 v_r}{\partial r^2} + \frac{\partial^2 v_r}{\partial z^2} = \frac{\partial \omega}{\partial z} - \frac{\partial}{\partial r}\left(\frac{v_z}{\rho}\frac{\partial \rho}{\partial z}\right) - \frac{\partial}{\partial r}\left(\frac{v_r}{r}\right) - \frac{\partial}{\partial r}\left(\frac{v_r}{\rho}\frac{\partial \rho}{\partial r}\right), \tag{2.4}$$

Axial Velocity

$$\frac{\partial^2 v_z}{\partial r^2} + \frac{\partial^2 v_z}{\partial z^2} = -\frac{\partial \omega}{\partial z} - \frac{\partial}{\partial z}\left(\frac{v_z}{\rho}\frac{\partial \rho}{\partial z}\right) - \frac{\partial}{\partial z}\left(\frac{v_r}{r}\right) - \frac{\partial}{\partial z}\left(\frac{v_r}{\rho}\frac{\partial \rho}{\partial r}\right), \tag{2.5}$$

Vorticity Transport

$$\begin{aligned} &r^2\left[\frac{\partial}{\partial z}\left(\frac{\omega}{r}\frac{\partial \psi}{\partial r}\right) - \frac{\partial}{\partial r}\left(\frac{\omega}{r}\frac{\partial \psi}{\partial z}\right)\right] - \frac{\partial}{\partial r}\left[r^3\frac{\partial}{\partial r}\left(\mu\frac{\omega}{r}\right)\right] \\ &-\frac{\partial}{\partial z}\left[r^3\frac{\partial}{\partial z}\left(\mu\frac{\omega}{r}\right)\right] = r\left[-rg\frac{\partial \rho}{\partial r} - r\nabla\left(\frac{v_r^2 + v_z^2}{2}\right)\cdot \mathrm{iso}(\rho)\right], \end{aligned} \tag{2.6}$$

Species

$$\begin{aligned} &\rho v_r \frac{\partial Y_k}{\partial r} + \rho v_z \frac{\partial Y_k}{\partial z} + \frac{1}{r}\frac{\partial}{\partial r}\left(r\rho Y_k V_{kr}\right) + \frac{\partial}{\partial z}\left(\rho Y_k V_{kz}\right) - \\ &W_k(\dot{w}_k + \dot{w}_k^s) = 0, \qquad k = 1, 2, \ldots, K, \end{aligned} \tag{2.7}$$

Sections

$$\begin{aligned} &\rho v_r \frac{\partial Y_k}{\partial r} + \rho v_z \frac{\partial Y_k}{\partial z} + \frac{1}{r}\frac{\partial}{\partial r}\left(r\rho Y_k (V_{kr}^s + V_{Tr})\right) + \frac{\partial}{\partial z}\left(\rho Y_k (V_{kz}^s + V_{Tz})\right) \\ &-\dot{q}_k = 0, \qquad k = K+1, K+2, \ldots, K+M, \end{aligned} \tag{2.8}$$

Energy

$$\begin{aligned} &c_p\left(\rho v_r \frac{\partial T}{\partial r} + \rho v_z \frac{\partial T}{\partial z}\right) - \frac{1}{r}\frac{\partial}{\partial r}\left(r\lambda\frac{\partial T}{\partial r}\right) - \frac{\partial}{\partial z}\left(\lambda\frac{\partial T}{\partial z}\right) + \\ &\sum_{k=1}^{K} \rho c_{p_k} Y_k\left(\frac{\partial T}{\partial r}V_{kr} + \frac{\partial T}{\partial z}V_{kz}\right) + \sum_{k=1}^{K} h_k W_k(\dot{w}_k + \dot{w}_k^s) - \nabla \cdot q_r = 0, \end{aligned} \tag{2.9}$$

Equation of State

$$\rho = \frac{p\overline{W}}{RT}. \tag{2.10}$$

The system is closed with appropriate boundary conditions on each side of the computational domain. For a confined coflowing flame we have

Axis of Symmetry ($r = 0$):

$$v_r = \frac{\partial v_z}{\partial r} = \frac{\partial \omega}{\partial r} = \frac{\partial Y_k}{\partial r} = \frac{\partial T}{\partial r} = 0, \quad k = 1, 2, \ldots, K + M, \tag{2.11}$$

Exit ($z \to \infty$):

$$v_r = \frac{\partial v_z}{\partial z} = \frac{\partial \omega_r}{\partial z} = \frac{\partial Y_k}{\partial z} = \frac{\partial T}{\partial z} = 0, \quad k = 1, 2, \ldots, K + M, \tag{2.12}$$

Inlet ($z = 0$):

$r < R_I$

$$\begin{aligned} v_r &= 0, \\ v_z &= v_F, \\ \omega &= \frac{\partial v_r}{\partial z} - \frac{\partial v_z}{\partial r}, \\ Y_k &= Y_{k_F}, \quad k = 1, 2, \ldots, K + M, \\ T &= T_F, \end{aligned} \tag{2.13}$$

$R_I < r < R_O$

$$\begin{aligned} v_r &= 0, \\ v_z &= v_{OX}, \\ \omega &= \frac{\partial v_r}{\partial z} - \frac{\partial v_z}{\partial r}, \\ Y_k &= Y_{k_{OX}}, \quad k = 1, 2, \ldots, K + M, \\ T &= T_{OX}, \end{aligned} \tag{2.14}$$

Wall ($r = R_O$):

$$\begin{aligned} v_r &= v_z = 0, \\ \omega &= \frac{\partial v_z}{\partial r}, \\ \frac{\partial Y_k}{\partial r} &= 0, \quad k = 1, 2, \ldots, K + M, \\ T &= T_{wall}. \end{aligned} \tag{2.15}$$

The subscripts I and O refer to the inner jet and the outer jet, respectively, and v_F, v_{OX}, $Y_{k_F}, Y_{k_{OX}}, T_F, T_{OX}$ and T_{wall} are specified quantities.

In addition to the variables already defined, K represents the total number of gas phase species and M, the number of soot (size) sections; T, denotes the temperature; Y_k, the mass fraction of the k^{th} gas-phase species ($k \leq K$) or the $(k-K)^{th}$ soot size class ($k > K$); p, the pressure; v_r and v_z, the velocities of the fluid mixture in the radial and axial directions, respectively; ρ, the mass density; W_k, the molecular weight of the k^{th} species; $\overline{W}$, the mean molecular weight of the mixture; R, the universal gas constant; λ, the thermal conductivity of the mixture; c_p, the constant pressure heat capacity of the mixture; c_{pk}, the constant pressure heat capacity of the k^{th} species; $\dot{w}_k$, the molar rate of production of the k^{th} species per unit volume; $\dot{w}_k^s$, the molar rate of production of the k^{th} species per unit volume due to scrubbing/replenishment by the soot growth/oxidation processes; $\dot{q}_k$, the rate of change of section k due to inception, surface growth, oxidation and coalescence; h_k, the specific enthalpy of the k^{th} species; g, the gravitational constant; μ the viscosity of the mixture; V_{k_r} and V_{k_z}, the diffusion velocities of the k^{th} species in the radial and axial directions, respectively; $V_{Tr}, V_{Tz}, V_{kr}^s, V_{kz}^s$, sectional thermophoretic and diffusion velocities of the k^{th} soot size class and $\nabla \cdot q_r$ the divergence of the net radiative flux for gas bands and soot in the optically-thin limit.

We write the diffusion velocities in the r and z directions in the form

$$V_{k_r} = -(1/X_k) D_k \frac{\partial X_k}{\partial r}, \quad k = 1, 2, \ldots, K, \tag{2.16}$$

$$V_{k_z} = -(1/X_k) D_k \frac{\partial X_k}{\partial z}, \quad k = 1, 2, \ldots, K, \tag{2.17}$$

where X_k is the mole fraction of the k^{th} species and D_k is related to the binary diffusion coefficients through the relation (see, e.g., Curtiss and Hirschfelder, 1949)

$$D_k = \frac{(1 - Y_k)}{\sum_{j \neq k}^{K} X_j / \mathcal{D}_{jk}}. \tag{2.18}$$

The sectional thermophoretic velocities in the free molecule regime are given by (Hall *et al.*, 1997)

$$V_{Tr} = -0.55 \frac{\mu}{\rho} \frac{1}{T} \frac{\partial T}{\partial r}, \tag{2.19}$$

$$V_{Tz} = -0.55 \frac{\mu}{\rho} \frac{1}{T} \frac{\partial T}{\partial z}. \tag{2.20}$$

The sectional diffusion velocities are written as in (2.16-2.17) with a mass weighted mean diffusion coefficient for each bin (Hall *et al.*, 1997). The binary diffusion coefficients, the viscosity, the thermal conductivity of the mixture, the chemical production rates and the thermodynamic quantities were evaluated using vectorized and highly optimized transport and chemistry libraries (Giovangigli and Darabiha, 1987).

Anticipating that radiative losses could have a significant influence on soot levels compared to a nonradiative system, we have included an optically-thin radiation model in our

calculations (Hall, 1993, 1994). We assume that for methane-air mixtures the only significant radiating species are H_2O, CO, CO_2 and soot. By utilizing an optically-thin limit in which self-absorption of radiation is neglected, the divergence of the net radiative flux can be written

$$\nabla \cdot q_R = C f_v T^5 + 4\pi \sum_{ik} \alpha_{ik} \rho_k I_{b_{ik}}, \tag{2.21}$$

where f_v is the soot volume fraction and $I_{b_{ik}}$ is the Planck function evaluated at the gas band centers of the contributing vibration-rotation or pure rotational bands whose integrated intensities are given by α_{ik}. The value of C is taken to be 4.243E-10 (giving a power density in watts/cc for T in Kelvin), and was derived from Grosshandler (1993).

3. Experimental Methods

3.1 Burner and Reactants

Atmospheric pressure, overventilated, axisymmetric, coflowing, nonpremixed laminar flames were generated with a burner in which the fuel flows from an uncooled 12 mm diameter vertical brass tube and the oxidizer flows from the annular region between this tube and a 102 mm diameter concentric tube (see Figure 1). Details of the burner construction and operation are given elsewhere (McEnally and Pfefferle, 1997). The oxidizer was air (710 cm^3/min), while the fuel was a mixture containing methane (240 cm^3/min) and argon (2.4 cm^3/min). The added argon aided species measurements as discussed below. All flowrates were governed by electronic mass flow controllers and are estimated to be accurate to within 5%.

3.2 Temperature and Soot Volume Fraction Measurements

Temperatures were measured with uncoated 75 μm wire-diameter type R thermocouples. By measuring profiles in coflowing flames with various size thermocouples, we have determined that while conduction errors of up to 100K occur at some flame locations with 125μm wires, they are negligible with 75 μm wires (McEnally *et al.*, 1997). The measured junction temperatures were converted to gas temperatures with a heat balance (radiation energy loss = convection energy gain) and the following parameters: Nusselt number = 2.26, junction diameter = 240 μm (measured with a microscope), temperature-dependent thermal conductivity data for air (Holman, 1986), and temperature-dependent type S thermocouple emissivities (Bradley, 1961). We estimate that the absolute error in the gas temperatures is less than 50K in soot-free flame regions. In soot-containing flame regions, particles rapidly deposit onto the junction, rendering the junction diameter and emissivity values listed above incorrect. Therefore the junction was cleaned before every measurement by retracting it into the oxidizing layer outside the flame, and the temperature was recorded quickly (0.75 seconds) after the junction was reinserted into the flame.

Soot volume fractions were measured with a new technique, thermocouple particle densitometry (TPD), that was suggested by Eisner and Rosner (1985) and recently implemented by McEnally *et al.* (1997). A clean thermocouple was introduced into the flame and its junction temperature was recorded periodically for 200 seconds; the soot volume fraction was then determined by optimizing the agreement between the measured history and one calculated with the thermophoretic mass transfer formulation of Eisner and Rosner (1985). In the work cited above we demonstrated that TPD measurements agreed with soot volume fractions measured by the conventional technique of laser extinction in counterflow and coflowing nonpremixed flames. We developed TPD and employed it here because the combination of low soot volume fractions (<1 ppm) and short pathlengths (<5 mm) make laser extinction measurements difficult in methane coflowing flames (Garo *et al.*, 1986), (Shaddix *et al.*, 1994). With TPD, soot volume fractions can be easily measured down to at least 0.02 ppm by allowing sufficient time to pass for a measurable change in the junction temperature to occur. The technique also allows spatially-resolved measurements without tomographic reconstruction. The results have an absolute accuracy of $\pm$ 50% and a relative accuracy of $\pm$ 10%.

Recent experiments have shown that nonpremixed flames contain two kinds of soot particles: an early type that appears translucent when viewed under an electron microscope, and a later type that appears dark (Mergaridis and Dobbins, 1989). Similarly, two types of particles have been identified in premixed flames, where the early particles were shown to be transparent to visible light (d'Alessio *et al.*, 1992). Results from our laboratory suggest that soot volume fractions measured by TPD include both particle types, while laser extinction and laser-induced incandescence respond to only the dark particles (McEnally and Pfefferle, 1996), (Köylü *et al.*, 1996).

3.3 Species Measurements

Species concentrations were measured by extracting gases from the flames with a narrow-tip quartz microprobe, and analyzing them with on-line mass spectrometry. The sampling procedure and its performance are discussed in greater detail in McEnally and Pfefferle (1997) where it was concluded that the microprobe spatial resolution was roughly one millimeter, reactions in the microprobe tip have only a minor affect on the measured concentrations, and condensation/adsorption losses to the sample manifold walls were insignificant for biphenyl ($C_{12}H_{10}$; 154 AMU) and all lighter species. Following Puri (1992), we have equipped the probe with an oscillating sapphire fiber that extends through its orifice and grinds down any soot deposits that accumulate there. This prevents complete clogging of the orifice, enabling us to make measurements in particle-containing flame regions.

Most species were quantified with a custom-built photoionization/time-of-flight mass spectrometer (PTMS) that can simultaneously measure all C_3 and larger hydrocarbons

(except propane and butane) with part-per-million detection limits (Bermudez and Pfefferle, 1995). This instrument generates ions via single-photon photoionization with a low-intensity vacuum-ultraviolet (118.2 nm) laser beam. Benzene concentrations were directly calibrated and are accurate to within a factor of two.

A commercial electron-impact/quadrupole mass spectrometer (EQMS; Leybold Inficon Transpector C100M) was used to measure methane, acetylene, and argon. The EQMS ionizes target gases with a fixed-energy 70 eV electron gun, which produces extensive ion fragmentation. Methane was measured with its CH_3^+ fragment-ion to avoid interferences from the O^+ fragment-ions of water and carbon dioxide, argon with its Ar^{++} ion to avoid interferences from $C_3H_4^+$ ions, and acetylene with its parent ion. The methane and acetylene concentrations were directly calibrated and are accurate to within 50%. However, ethylene fragment ions may account for up to 30% of the acetylene signal; ethylene and its $C_2H_3^+$ fragment-ion were completely obscured by nitrogen at all flame locations, so only an upper bound of 2000 ppm could be determined for its mole fraction.

The flowrate into the microprobe varied with flame position due to changes in the gas temperature and partial clogging of the orifice. To account for this, all PTMS and EQMS mass spectra were normalized with the EQMS argon signal by assuming that the argon concentration was uniform throughout the flame. As mentioned above, argon was added to the fuel so that its concentration was 1% in both reactant streams. At a height close to the burner surface, where soot clogging was insignificant, the radial temperature profile could be recovered from the raw argon signals, indicating that the constant-argon assumption is valid.

4. Numerical Method

Our goal is to obtain a discrete solution of the two-dimensional, elliptic, governing conservation equations for the temperature, gas-phase and soot mass fractions, velocities and vorticity on a two-dimensional mesh the initial nodes of which are formed by the intersection of the lines of the mesh $\mathcal{M}_r$

$$\mathcal{M}_r = \{0 = r_0 < r_1 < \ldots < r_i \ldots < r_{M_r} = R_O\}, \tag{4.1}$$

and the mesh $\mathcal{M}_z$

$$\mathcal{M}_z = \{0 = z_0 < z_1 < \ldots < z_j \ldots < z_{M_z} = Z\}. \tag{4.2}$$

Computationally, we combine a steady-state and a time-dependent solution method. A time-dependent approach is used to help obtain a converged numerical solution on an initial coarse grid. Grid points are then inserted adaptively and Newton's method is used to complete the problem. Specifically, the spatial operators in the governing partial differential equations are approximated by finite difference expressions. Diffusion terms

are approximated by centered differences and convective terms by upwind approximations. With the difference equations written in residual form, we seek the solution U^* of the system of nonlinear equations

$$F(U) = 0. \tag{4.3}$$

For an initial solution estimate U^0 which is sufficiently close to U^*, the system of nonlinear equations in (4.3) can be solved by Newton's method. This leads to the iteration

$$J(U^n)(U^{n+1} - U^n) = -\lambda^n F(U^n), \quad n = 0, 1, 2, \ldots. \tag{4.4}$$

where $J(U^n) = \partial F(U^n)/\partial U$ is the Jacobian matrix and λ^n $(0 < \lambda \leq 1)$ is a damping parameter.

We point out that with the spatial discretizations used in forming (4.3), the Jacobian matrix in (4.4) can be written in block-nine-diagonal form. We form several columns of the Jacobian simultaneously using vector function evaluations and the Jacobian's given sparsity structure. The Newton equations are solved by a preconditioned BiCGSTAB iteration. The Newton iteration continues until the size of $\|U^{n+1} - U^n\|_2$ is reduced appropriately. Grid points of the two-dimensional mesh are determined by equidistributing positive weight functions over mesh intervals in both the r and z directions. During the pseudo-transient portion of the calculation, the size of the time steps is chosen by monitoring the local truncation error of the time discretization process. Due to the cost of forming the Jacobian matrices with detailed transport and finite rate chemical kinetics, a modified Newton method is implemented along with several theoretical estimates that determine when a new Jacobian should be reformed. These theoretical results help increase the overall efficiency of the algorithm (see Smooke *et al.*, 1990, 1996 for more details).

5. Results and Discussion

In this section we apply the model, solution procedure, and experimental methods discussed in Sections 2, 3 and 4 to a confined, axisymmetric, coflow, methane-air diffusion flame with the goal of helping to interpret flame structure and soot formation phenomena. Initial modeling results were compared with the experimental values for bulk flame parameters; i.e., flame height, peak flame temperatures, etc. Initially, flame height was overpredicted by the model by 15% and temperatures were underpredicted by about 100-150K. This lack of agreement was considered unacceptable. Upon analysis of both the model and the experiment, it became apparent that conduction/radiation from the base of the flame to the burner exit tube in the experiment caused noticeable preheating of both inlet fuel and air streams. Calculations demonstrated that the flame height and local temperatures were significantly affected by these assumed inlet temperatures. Increasing the inlet temperatures from 300 to 420K (mass flow held constant) provided better agreement

to the flame height and local temperatures (see later discussion). This approach, while not perfect, offers a tractable computational solution to a challenging problem. This increment is consistent with attempts to measure the temperature at the burner exit plane. The computational results demonstrate the importance of accurate specification of initial conditions, specifically temperature (and resultant effects on local velocities), on the numerical solutions.

Time-stepping from nearly converged solutions led to the build up of large soot particles at the base of the flame in the wake of the burner lip. Neither surface growth nor inception can produce soot in this low temperature region. Several numerical experiments demonstrated that the source of this build-up was thermophoresis. Small soot particles generated a little further from the lip (at higher temperatures and inside the flame front) were driven inside this small wake due to large temperature gradients. Coalescence of these small particulates, continually fed into the wake region over long computation times, led to the formation of large particles which were not flushed away by the flow. In heavier sooting co-flow flames, such build-up with time has been observed experimentally as evidenced by the occasional requirement to shut down and clean particulates from the exit tube (Santoro, 1996). This build-up is not observed experimentally for the lightly sooting methane flame. This process has been suppressed in the model by setting the thermophoretic velocity to zero below 750K. This empirical correction does not cause any noticeable change of predicted soot levels in the remainder of the flow field.

The chemical kinetic mechanism used in this work was derived from GRIMech 2.11 with its recommended thermodynamics (Bowman *et al.*, 1995). Modifications of the mechanism included removal and addition of reaction paths which are believed to have a minimal impact on the bulk chemistry in the system. All reactions related to NO formation and other odd nitrogen species were stripped from the set. In addition, a series of reactions related to the formation and oxidation of benzene, and related species, were included (see Table 1 of Hall *et al.*, 1997). The dominant ring forming reaction was propargyl recombination. This is consistent with material balance analyses of benzene formation mechanisms based on the experimental species concentrations. The burner fuel tube had an inner radius of R_I=0.5556 cm with a wall thickness of 0.0794 cm. The radius of the coflow was $R_O = 4.7625$ cm. Conditions at the fuel and oxidizer jet inlets (plug flow) were such that

$$v_F = 5.52\text{cm/sec}, \quad v_{OX} = 12.54\text{cm/sec}, \tag{5.1}$$

$$T_F = 420\text{K}, \quad T_{OX} = 420\text{K}. \tag{5.2}$$

All calculations were performed on an IBM RS/6000 Model 590 computer. In the computations to be presented 12 soot size classes were included in the model. Starting from a converged solution for a methane-air flame without the sectional equations, we typically obtained converged solutions for the complete gas-soot problem in several hours of

computer time.

Temperature Predictions

Examination of the curves in Figure 2 demonstrates that the model predicts the general shape and structure of the flame (location of peak flame temperatures, etc.) reasonably well. Temperature is perhaps the most important of the flame parameters as temperature has a direct influence on virtually all the other flame properties (e.g., flame height and width, species concentrations, soot, etc.) A more careful comparison of the profiles in Figure 2 shows that the model underpredicts the experimental measurements along the centerline by about 100 K at all heights within the flame. In addition, while the location and value of the peak temperature are reasonably well described up to about a height of z = 2 cm, temperatures are overpredicted at the outside edge (i.e., predicted temperatures do not fall off as rapidly as the data with increasing radius). Finally, the experimental flame closes to the centerline (at $z \approx 40$ mm) more rapidly than does the computed flame. The computed low centerline temperatures and the delayed contraction of the flame tip, presumably, are very much related to the inability to match accurately the flame height. These deficiencies in the model are attributable, at least partly, to the uncertainties in the inlet boundary conditions. As argued below, these limitations of the computed temperature field influence the prediction of gas species and particulates. One possible explanation of the low temperatures along the centerline is the lack of inclusion in the model of absorption by methane of energy radiated from the flame front.

Prediction of Species

Figure 3 shows comparison of the methane profiles as a function of radius at several heights above the burner. Again the general features of the radial profiles are reproduced well by the model. Typically, methane is overpredicted by a factor of two along the centerline. This result is consistent with lower temperatures and a taller computed flame. Alternatively, the model overpredicts the fall-off with increasing radius, most noticeably at the lowest height, $z = 1.0$ cm. This accentuated fall-off is undoubtedly a direct result of the higher predicted temperatures in the wings of the flame, and hence more rapid chemistry. The factor of three overprediction at $z = 2.5$ cm on the centerline, is a consequence of the (experimental) rapid decrease in methane concentration in this region of the flame, i.e., the flame tip, and the inability to match the flame height exactly.

Similar comments can be made in regard to the acetylene and benzene profiles (Figures 4 and 5). In these cases, however, centerline values are underpredicted, presumably because methane decomposition is suppressed at the low predicted temperatures along the centerline, as discussed above. Not surprisingly, the relatively small underprediction of acetylene (factor of two) along the centerline, leads to a larger deficit in the computed benzene profiles (a factor of three) on the centerline. Since these species are key to the growth and inception of particulates, the combination of their low values as well as the

low temperature predictions along the centerline must lead commensurately to low predictions of soot in these regions. Of importance, however, is that the concentrations of these species, as well as temperatures, are better described in the flame front region most critical to inception and growth. Until a satisfactory solution is found to predict more accurately centerline temperatures, quantitative predictions of formation of the translucent droplets/particles along the centerline, such as observed by Megaridis and Dobbins (1989) will likely not be achieved.

Soot Particulates

Figure 6 depicts the computed and measured values of the soot volume fraction (cm^3 soot/cm^3 gas) as a function of radius at z = 2.0, 2.25, 2.5 and 2.75 cm. As with the species profiles, the computations describe the general features of the soot field. Peak soot volume fractions are underpredicted by a factor of about three, but the shape of the soot volume fraction profile and its shift towards the centerline with increasing z is reproduced well. The experimental peak values collapse to the centerline more rapidly, as discussed above, because of the difference in the computed flame height. Centerline values are significantly underpredicted (order of magnitude) because of the combination of predicted low temperatures (100K), low acetylene (factor of two) and low benzene (factor of three). It is reasonable to assume that should these bulk flame properties be more accurately modeled, our ability to attain quantitative predictions of the soot field would be enhanced dramatically.

Predicted soot volume fractions are strongly dependent on predicted acetylene profiles, which generally are dependent upon the kinetics supplied by GRIMech, but also are depressed when scrubbing is included in the calculations. Without the added chemical mechanisms and soot formation steps, predicted levels of acetylene are very close to the experimental values, depending on the flame location. Measured peak acetylene concentrations are about 12,000 ppm. The measured peak soot volume fractions are 4.7×10^{-7} which is approximately equivalent to 4000 ppm acetylene. Hence, suppression of the acetylene peak by the soot formation is expected and is observed in these calculations – even in these lightly sooting flames. The reduced acetylene levels, in turn, suppress the levels of soot predictions, since both the inception and the growth processes are strongly dependent on the acetylene concentration. Predicted acetylene concentrations more consistent with experimental results would result in more favorable agreement between predicted and measured soot volume fraction in Figure 6. Soot volume fraction predictions based on this growth model have some residual sensitivity to the number of size classes at the value of 12 employed, which was the largest number permissible given the number of species and grid nodes relative to available computer memory. While size class convergence will have to be addressed ultimately, factors such as inlet/boundary conditions and flame chemistry may have a much greater influence on the accuracy of the solution and its ability to reproduce bulk flame parameters (specifically, temperature). As will be seen, calculations with

another soot growth model show much more rapid convergence with the number of size classes.

2D Representations

In Figures 7a-d and 8a we illustrate contour plots of the same variables plotted in Figures 2-6. The two-dimensional, color contour of computed temperatures in Figure 7a clearly shows the peak temperature regions in the flame front. The highest temperatures within the flame are not at the flame peak, but in the outer annulus regions. Peak height can be inferred from these profiles by locating the point at which the temperature peaks on the centerline, for example. The contour plot of methane shows a dramatic loss of methane very low in the flame. This extremely rapid decay is principally due to the rapid diffusion of molecular nitrogen to the centerline, rather than the reaction of methane. (In fact, it is exactly this rapid diffusional process that has led to confusion in the literature when attempts have been made to separate dilution from temperature effects and their relative importance to soot formation.). Predicted peak acetylene and benzene profiles occur on the centerline about a centimeter below the flame tip near $z = 2.8$ cm. Benzene seems to decay more rapidly above this location than does acetylene. The rapid decay in the acetylene appears more closely aligned with the flame tip. Alternatively, the earlier decay in the benzene is linked to the soot inception process, which attains its peak rates in this region of the flame.

Soot Growth and Inception

Figures 8b-d contain contour plots of the net soot production, soot inception and soot oxidation, respectively. Comparison of the net soot production (Figure 8b) with inception (Figure 8c) shows that the growth region is surface- rather than inception-dominated. Higher in the flame net growth gives way to oxidation as the particles burn out (Figure 8d). The surface growth contours are a convolution of the temperature and acetylene contours (Figures 7a and 7c), strongly reflecting the annular shape of the temperature profile, while inception is an image of the benzene contour of Figure 7d.

Soot Oxidation

The rates of oxidation of the particulates by OH are shown in Figure 8d. Maximum oxidation rates by O_2 (not shown here) are about a factor of 5 to 10 below those by OH. Oxidation by O_2 occurs in two separate regions of the flow. Near the base of the flame, O_2 diffuses underneath the flame and contributes to soot oxidation on the fuel-rich side of the flame, but these oxidation rates are low due to the limited oxygen supply. O_2 also contributes to soot oxidation in the post flame region, but again at low rates since OH has already consumed the majority of the particulates as they pass through the flame front. The hydroxyl radical is clearly the dominant oxidizing species in this flame. Peak oxidation rates occur in the conventional wing tips of the flame and high oxidation rates

continue to the centerline. These results (i.e., the strong dominance of OH as the principal oxidizing species) are wholly consistent with those of Garo, *et al.* (1990) who analyzed the dynamics of a methane-air coflow diffusion air and more recently of Kennedy, *et al.* (1996) in their detailed modeling of an ethylene coflow diffusion flame. Together, the present and prior results cast doubts on the validity of models which neglect the role of oxidation by OH in coflow flames (for example, Kaplan, *et al.* (1996) and Sivanthanu and Gore (1994)). The cause of the high importance of OH as the principal oxidizing species is its high superequilibrium level in the flame front. (See discussion below.)

In this study, the soot field has been modeled using a constant 0.13 collision frequency for reaction after Neoh, *et al.* (1981). In the Kennedy, *et al.* (1996) study, this reaction efficiency was varied linearly from 0.05 low in the flame to 0.2 in the tip flame region, to assist in matching soot profiles. In addition, Garo, *et al.* interpreted their data to be consistent with a varying collision frequency with height in the flame. While it is apparent that such methods could assist matching the experimental and modeling profiles of soot, we have not yet adopted this approach.

Superequilibrium OH

Smooke, et al. (1992) have computed superequilibrium levels of hydroxyl in methane air coflow flames. Santoro and coworkers (1994) have measured OH concentrations and temperatures in ethylene flames and found these radical concentrations to be affected by the level of soot in the flame. They argued that high oxidization rates of soot decreased OH concentrations. Such effects were not noticeable in this study, presumably due to the much lower concentrations of soot. The OH measured by Puri, Santoro and Smyth (1994) were described to be at superequilibrium levels. To examine levels of superequilibrium in the present study, calculated OH (referred to here as "flame OH" have been compared to the equilibrium levels of OH based on 1) the local temperature (constant temperature calculation), 2) the full equilibrium (constant enthalpy calculation), and 3) a partial equilibrium assumption based on

$$O_2 + H_2 \leftrightarrow 2OH$$

and the local flame temperature. The ratio of this flame OH to the equilibrium levels are plotted in Figure 9 as a function of the radius at $z = 4.01$ cm. The maximum soot oxidation rate occurs at this height at a radius of about 0.31 cm. At this radius, the OH attains concentrations a factor about 10 above the equilibrium value, thus validating further the existence of large OH superequilibrium concentrations as an important contributor to the destruction/burnout of soot. Chemical systems which cannot support such high superequilibrium levels may be more prone to soot emissions. The partial equilibrium assumption (assuming knowledge of the H2, O2 concentrations and temperature) provides a much better estimate of hydroxyl, at least through the flame front region where soot is being oxidized.

Particle Size

Figure 10a-d shows the evolution of soot particle size distribution in space as a result of surface growth and coalescence. The sectional mass boundaries have been placed linearly on a logarithmic scale. Peak soot mass concentration occurs in size class nine, whose mass-weighted mean diameter is about 48 nm, which should be considered an estimate. A larger number of sections than that employed here would be required to obtain an accurate average particle size. This average size is clearly larger than typical determinations of 20-30 nm in laboratory flames and suggests some refinements in our soot model are still required. The fact that the suspended mass in the highest class remains relatively small shows that the upper boundary of the particle size domain has been set high enough to avoid unphysical accumulation of particles in the highest size class. The smallest size classes are observed to disappear rapidly in the post flame zone, while a portion of the largest particles survive to the end of the computational domain.

Particle size distribution within the flame can also be visualized from Figures 11a and 11b in which the mass fractions of each of the 12 soot mass classes (mc) are plotted as a function of radial distance for heights of 1 and 3 centimeters. Low in the flame, the sixth soot class contains the peak mass fraction and at 3 cm (just before the onset of rapid soot oidation by OH inside the flame front), the maximum occurs in the ninth class. At this higher position, substantial soot is found also near the centerline of the flame. However, the average particle for this "centerline" soot is much smaller than that just inside the flame front, a result qualitatively consistent with the results by Megaridis and Dobbins (1989). Since benzene concentrations (Figure 7d) and hence inception rates (see Figure 8c) are peaking in this region of the flow, the particles depicted on the centerline are likely formed along or near to the centerline rather than transported via thermophoresis from the flame front to this centerline region.

Radiation Effects

While it might be expected that thermal radiation effects would be small in a lightly sooting flame like that investigated here, simulations in which the radiative loss term, Eq. 2.21, is set equal to zero show that radiation effects are significant. Without radiation, predicted peak temperatures are 122K higher, a change large enough to affect predicted soot levels and species concentrations. Predicted peak volume fractions increase by a factor of three, with peak acetylene and benezene levels increasing by 45% and 22%, respectively. The significance of thermal radiation in this lightly sooting flame arises from residence times that are relatively long compared to those for counterflow diffusion flames, in which radiation effects are significant only for extremely low strain rates (Garcia, et al., 1996). With the relatively low values of soot concentration and the fact that the soot does not occupy the peak temperature regions, the thermal radiation in the experiment is estimated to have comparable contributions from the gas (water vapor and carbon dioxide)

and the soot. In the simulations, where the predicted soot levels are lower, the radiation is dominated by the molecular species. The physical dimensions of this flame are sufficiently small that self-absorption or optical thickness corrections should be minimal.

Variations of Inlet Gas Temperatures

Early modeling efforts with the inlet gas temperatures at 298K resulted in a flame height about 15% higher than the experimental value. In addition, predicted peak flame temperatures were about 125K below the experimental value. Since soot volume fractions are a strong function of temperatures, these low predicted temperatures substantially limited our ability to predict accurately the soot concentrations. Local temperatures in the unburned gases just above the burner lip were measured to be much higher than 298K, presumably due to radiation preheating and conduction. Accurate treatment of this problem would require knowledge not only of temperatures, but also of local velocities at each location in the burner inlet. To 1) analyze this problem in a simplified manner, 2) provide information relative to a sensitivity study, and 3) elevate the peak flame temperatures to values closer to the experimental levels, calculations were performed for elevated temperatures in the entire fuel flow, the entire air flow, or both streams. For each case, the mass flows per unit area were held constant and hence velocities increased with higher temperatures.

Table 1 compares the peak soot volume fractions and the peak flame temperatures obtained for several solutions at inlet temperatures ranging from 298 to 500K. An examination of these numbers demonstrates that an increase in the air temperature has a much more dramatic effect on both the peak flame temperature and volume fraction than comparable changes in the fuel temperature. Presumably, this effect is due to the higher mass weighted enthalpy content of air under stoichiometric conditions. The higher flame temperatures which arise from the elevated inlet air temperatures lead to a proportionally greater increase in the soot generation.

Comparisons to Fairweather, et al. model

Finally, the model was rerun with the inception and surface growth model of Fairweather *et al.* (1992). Soot volume fraction, net soot production, inception, and oxidation are illustrated in Figures 12a-d. In this model, which has been applied to ethylene- and acetylene-fuelled coflow flames (Kennedy, 1996; Sivathanu and Gore, 1994), both inception and surface growth are proportional to acetylene concentration. Its inception and surface growth rates are used here in the polydisperse, sectional representation rather than the monodisperse representation of the original model. Additionally, oxidation by OH, not included in Fairweather, et al. (1992), has been accounted for in this implementation.

TABLE 1

Effect of Fuel and Oxidizer Inlet Temperatures on
Peak Soot Volume Fraction and Peak Flame Temperature

T_f/T_{ox}	f_v	T_{max}
298/298	3.30×10^{-8}	1942 K
298/420	8.71×10^{-8}	1976 K
298/500	1.43×10^{-7}	2000K
420/298	4.67×10^{-8}	1948 K
500/298	5.87×10^{-8}	1954 K
420/420	1.14×10^{-7}	1984 K
500/500	1.56×10^{-7}	2005 K

The predicted soot concentrations (Figure 12a) are seen to be slightly larger than those predicted with the base model. Given the previously discussed uncertainties associated with the chemical mechanism and burner boundary conditions, however, no judgements about the merits of this model vis-a-vis the base model are warranted. Inception is more significant in the Fairweather, et al. (1992) model (compare Figures 12c and 8c), and this seems to give calculations using it much less sensitivity to the number of soot sections employed. Predicted soot volume fractions using five and twelve sections were not significantly different. The spatial distribution of inception in the two models is very different, as Figures 8c and 12c show. The Fairweather, et al. (1992) model has an inception profile that is strongly annular, reflecting, like the surface growth, the convolution of temperature and acetylene profiles. Oxidation in this latter model is also dominated by OH.

Summary of Differences Betweeen Model and Experiment

Differences between our predictions and the experimental data include: overprediction of flame height, underprediction of peak temperatures, too slow decay of methane along the centerline and a slow decay of temperature in the wings of the flame. In addition, the model significantly underpredicts the peak soot volume fractions in the flame and tends to overpredict particle size. Much of the differences can be directly linked to the inadequate prediction of the temperature field and the flame height. Contrasting these results are the very good agreement of the temperature field and flame height obtained in the modeling of a methane coflow flame in a study of NO formation Smooke, et al. (1997). Principal differences between this previous study and that of the present investigation includes dilution of the fuel, higher flow rates, and a lifted flame. We believe the most likely of these parameters affecting uncertainties in the present study is the inability of our code to properly model the attachment (i.e., close proximity) of the flame to the

burner lip and all of its attendant effects. Other possible contributors to this error include uncertainties in the kinetics. For example, using this kinetic mechanism (hydrocarbon portion of GRIMech 2.11) the extinction limit in a counterflow methane-air diffusion flame is significantly overpredicted (380 cm^{-1} experiments vs. predictions of 620 cm^{-1}). We note also that there are still fundamental uncertainties in soot growth modeling such as the rates of inception, surface growth, and coalescence of very small particles. For example, a 50% increase in the surface growth rate constant results in a predicted soot volume fraction in much better agreement with data. Until the temperature field is more accurately described, it is difficult to offer quantitative arguements about the accuracy (or lack thereof) of our soot model. Nevertheless, the qualitative results and conclusions should still be valid.

6. Conclusions

The axisymmetric laminar diffusion flame provides a natural environment in which one can investigate the interaction of soot formation with detailed gas-phase chemistry in a multidimensional system. In this paper we have compared experimental measurements of the temperature, soot volume fraction and selected species from an axisymmetric, laminar, methane-air diffusion flame with computational results obtained by generalizing the sectional model presented in Hall et al. (1997) to a coflow model. This work represents the first time that a detailed chemistry/complex transport flame model has been coupled to a polydisperse soot growth analysis in which the scrubbing of gaseous species and both gas and particle radiation are included. The detailed chemistry includes species up through benzene with a steady-state model for the formation of polyaromatic hydrocarbons to simulate soot inception. Unfortunately, descrepancies between the experimental data and the computed results for several bulk flame parameters (such as temperatures and flame height) limited the ability to quantitatively evaluate the overall validity of our model(s). Soot volume fractions calculated using either our growth/inception formulation or that by Fairweather et al. (1992) underpredicted the experimental values by about a factor of three. These low values are directly attributable to low predicted temperatures, leading to low computed values of critical growth species such as acetylene and benzene. Inaccuracies in the predicted temperature fields may be partially due to inadequate modeling of flame attachment at the burner lip.

Despite these descrepancies, several key conclusions can be extracted from this study. These results strongly support earlier studies indicating the importance of soot oxidation by hydroxyl radicals and is largely due to super-equilibrium levels of OH that are about a factor of ten above equilibrium. This work also confirms the importance of fully coupling radiation into the flow field solutions. Radiation loss reduces the peak temperatures by over 100K. Ignoring radiation leads to increases in concentrations of key soot growth/inception

species contributing to a factor of three increase in predicted soot volume fractions. Particle sizes are shown to vary significantly with location in the flame. Particle diameters grows much more slowly along the centerline of the flame, consistent with experimental measurements. Alternatively, while nearly all particles are consumed through the flame front in this 'non-sooting' coflow flame, a few small particles with large diameter (and low surface area) escape to be oxidized in the post-flame region. Finally, a comparison of two significantly different inception/growth models has led to good agreement between the predicted soot (volume fraction and spatial distribution).

Acknowledgments

This work has been supported in part by the Air Force Office of Scientific Research under contract F49620-94-C-0059 and the United States Department of Energy, Office of Basic Energy Sciences. The encouragement of Julian Tishkoff and discussions with R. J. Santoro (Penn State University), R. A. Dobbins (Brown University) and M. A. Tanoff (Yale University) are gratefully acknowledged. The assistance of R. R. Dobbins (Yale University) was essential in the preparation of the figures.

References

Axelbaum, R.L., Flower, W.L., and Law, C.K., "Dilution and Temperature Effects of Inert Addition on Soot Formation in Counterflow Diffusion Flames," *Combust. Sci. Tech.*, **61**, p. 51-73 (1988).

Bermudez, G., and Pfefferle, L.D., "Laser Ionization Time-of-Flight Mass Spectrometry Combined with Residual Gas Analysis for the Investigation of Moderate Temperature Benzene Oxidation," *Combust. Flame*, **100**, p. 41-51 (1995).

Bowman, C.T., Hanson, R.K., Davidson, D.F., Gardiner, Jr., W.C. Lissianski, V., Smith, G.P., Golden, D.M., Frenklach, M., Wang, H., and Goldenberg, M., *GRI-Mech version 2.11*, http://www.gri.org (1995).

Bradley, D., and Entwistle, A.G., "Determination of the Emissivity, for Total Radiation, of Small Diameter Platinum-10% Rhodium Wires in the Temperature Range 600–1450°C," *British Journal of Applied Physics*, **12**, p. 708-711 (1961).

Colket, M.B., and Hall, R.J., "Successes and Uncertainties in Modeling Soot Formation in Laminar, Premixed Flames," in *Soot Formation in Combustion, Mechanisms and Models*, H. Bockhorn, Ed., Springer Series in Chemical Physics **59**, Springer-Verlag, p. 442-470 (1994).

Colket, M.B., and Hall, R.J., "Mechanisms Controlling Soot Formation in Diffusion Flames," Annual Report for AFOSR Contract F49620-94-C-0059, August, 1995; Hall, R.J., (1996).

Curtiss, C.F., and Hirschfelder, J.O., "Transport Properties of Multicomponent Gas Mixtures," *J. Chem. Phys.*, **17**, p. 550 (1949).

D'Alessio, A., D'Anna, A., D'Orsi, A., Minutolo, P., Barbella, R., and Ciajolo, A., "Precursor Formation and Soot Inception in Premixed Ethylene Flames," *Twenty-Fourth Symposium (International) on Combustion*, The Combustion Institute, Pittsburgh, 1992, p. 973-980.

Eisner, A.D., and Rosner, D.E., "Experimental Studies of Soot Particle Thermophoresis in Nonisothermal Combustion Gases Using Thermocouple Response Techniques," *Combust. Flame*, **61**, p. 153-166 (1985).

Ern, A., Douglas, C.C., and Smooke, M.D., "Detailed Chemistry Modeling of Laminar Diffusion Flames on Parallel Computers," *Int. J. of Supercomputer Appl.*, **9**, p. 167 (1995).

Fairweather, M., Jones, W.P., and Lindstedt, R.P., "Predictions of Radiative Transfer from a Turbulent Reacting Jet in a Cross-Wind," *Combust. Flame*, **89**, p. 45 (1992).

Garcia, C., Tanoff, M. A., Smooke, M. D., and Hall, R. J., "Application of a Non-Optically Thin Radiation Model to the Study of Low-Strain Laminar Counterflow Flames," Eastern States Meeting of the Combustion Institute, Hilton Head, December, 1996.

Garo, A., Lahaye, J., and Prado, G., "Mechanisms of Formation and Destruction of Soot Particles in a Laminar Methane-Air Diffusion Flame," *Twenty-First Symposium (International) on Combustion*, The Combustion Institute, Pittsburgh, 1986, p. 1023-1031.

Garo, A., Prado, G., and Lahaye, J., "Chemical Aspects of Soot Particles Oxidation in a Laminar Methane-Air Diffusion Flame," *Combust. Flame*, **79**, p. 226-233 (1990).

Gelbard, F., and Seinfeld, J.H., "Simulation of Multicomponent Aerosol Dynamics," *J. Coll. Int. Sci.*, **78**, p. 485 (1980).

Giovangigli, V. and Darabiha, N., "Vector Computers and Complex Chemistry Combustion," in *Proceedings of the Conference on Mathematical Modeling in Combustion*, Lyon, France, NATO ASI Series (1987).

Grosshandler, W.L., "RADCAL: A Narrow-Band Model for Radiation Calculations in a Combustion Environment," NIST Technical note 1402 (1993).

Hall, R.J., "The Radiative Source Term for Plane-Parallel Layers of Reacting Combustion Gases," *J. Quant. Spec. Rad. Tran.*, **49**, p. 517 (1993).

Hall, R.J., "Radiative Dissipation in Planar Gas-Soot Mixtures," *J. Quant. Spec. Rad. Tran.*, **51**, p. 635 (1994).

Hall, R.J., Smooke, M.D., and Colket, M.B., "Predictions of Soot Dynamics in Opposed Jet Diffusion Flames," in *Physical and Chemical Aspects of Combustion: A Tribute to Irvin Glassman*, ed. by R.F. Sawyer and F.L. Dryer, Combustion Science and Technology Book Series, Gordon and Breach, (1997).

Harris, S.J., and Weiner, A.M., "Surface Growth of Soot Particles in Premixed Ethylene/Air Flames," *Combust. Sci. Tech.*, **31**, p. 155 (1983).

Harris, S.J., Weiner, A.M., and Blint, R.J., "Formation of Small Aromatic Molecules in a Sooting Ethylene Flame," *Combust. Flame*, **72**, p. 91-109 (1988).

Holman, J.P. Heat Transfer. McGraw-Hill Book Company, New York, 1986, p. 643.

Hura, H.S. and Glassman, I., "Soot Formation in Diffusion Flames of Fuel/Oxygen Mixtures," *Twenty-Second Symposium (International) on Combustion*, The Combustion Institute, Pittsburgh, 1988, p. 371.

Kaplan, C.R., Shaddix, C.R., and Smyth, K.C., "Computations of Enhanced Soot Production in Time-Varying CH_4/Air Diffusion Flames," *Combust. Flame*, **106**, p. 392 (1996).

Kennedy, I.M., Rapp, D.R., Santoro, R.J., and Yam, C., "Modeling and Measurements of Soot and Species in a Laminar Diffusion Flame," *Combust. Flame*, **107**, p. 368-382 (1996).

Kennedy, I.M., Kollmann, W., and Chen, J.Y., "Model for Soot Formation in a Laminar Diffusion Flame," *Combust. Flame*, **81**, p. 73-85 (1990).

Köylü, Ü.Ö., McEnally, C.S., Rosner, D.E., and Pfefferle, L.D., "Simultaneous Measurements of Soot Volume Fraction and Particle Size/Microstructure in Flames Using a Thermophoretic Sampling Technique," *Combust. Flame*, **110**, p. 494-507 (1997).

Leung, K.M., Lindstedt, R.P. and Jones, W.P., "A Simplified Reaction Mechanism for Soot Formation in Nonpremixed Flames," *Combust. Flame*, **87**, p. 289-305 (1991).

Lindstedt, P., "Simplified Soot Nucleation and Surface Growth Steps for Non-premixed Flames," in *Soot Formation in Combustion, Mechanisms and Models*, H. Bockhorn, Ed., Springer Series in Chemical Physics **59**, Springer-Verlag, p. 417-441 (1994).

Markatou, P., Wang, H., and Frenklach, M., "Computational Study of Sooting Limits in Laminar Premixed Flames of Ethane, Ethylene and Acetylene," *Comb. and Flame*, **93**, p. 467-482, (1993).

McEnally, C.S., and Pfefferle, L.D., "Aromatic and Linear Hydrocarbon Concentration Measurements in a Non-Premixed Flame," *Combust. Sci. Tech.*, **116–117**, p. 183-209 (1996).

McEnally, C.S., Köylü, Ü.Ö., Pfefferle, L.D., and Rosner, D.E., "Soot Volume Fraction and Temperature Measurements in Laminar Non-Premixed Flames Using Thermocouples," *Combust. Flame*, **109**, p. 701-720 (1997).

Megaridis, C.M., and Dobbins, R.A., "Comparison of Soot Growth and Oxidation in Smoking and Non-Smoking Ethylene Diffusion Flames," *Combust. Sci. Tech*, **66**, p. 1-16 (1989).

Neoh, K.G., Howard, J.B., and Sarofim, A.F., in *Particulate Carbon: Formation During Combustion*, D.C. Seigla and G.W. Smith, Eds., Plenum, New York, p. 261 (1981).

Puri, R. *The Interaction of Soot Particles and Carbon Monoxide in Laminar Diffusion Flames.* Ph.D. thesis, The Pennsylvania State University, 1992.

Puri, R., Santoro, R. J., and Smyth, K. C., *The Oxidation of Soot and Carbon Monoxide in Hydrocarbon Diffusion Flames*, *Combust. Flame*, **97**, p. 125-144 (1994).

Santoro, R.J., personal communication (1996).

Shaddix, C.R., Harrington, J.E., and Smyth, K.C., "Quantitative Measurements of Enhanced Soot Production in a Flickering Methane/Air Diffusion Flame," *Combust. Flame*, **99**, p. 723-732 (1994).

Sivathanu, Y.R., and Gore, J.P., "Coupled Radiation and Soot Kinetics Calculations in Laminar Acetylene/Air Diffusion Flames," *Combust. Flame*, **97**, p. 161 (1994).

Smooke, M.D., Mitchell, R.E. and Keyes, D.E., "Numerical Solution of Axisymmetric Laminar Diffusion Flames," *Combust. Sci. Tech.*, **67**, p. 85-122 (1989).

Smooke, M. D., Lin, P., Lam, J. K., and Long, M. B., "Computational and Experimental Study of a Laminar Axisymmetric Methane-Air Diffusion Flame," *Twenty-Third Symposium (International) on Combustion*, The Combustion Institute, Pittsburgh, 1990, p. 575-582.

Smooke, M.D., Xu, Y., Zurn, R.M., Lin, P., Frank, J.H. and Long, M.B., "Computational and Experimental Study of OH and CH Radicals in Axisymmetric Laminar Diffusion Flames," *Twenty-Fourth Symposium (International) on Combustion*, The Combustion Institute, Pittsburgh, 1992, p. 813-821.

Smooke, M.D., Ern, A., Tanoff, M.A., Valdati, B.A., Mohammed, R.K., Marran, D.F. and Long, M.B., "Computational and Experimental Study of NO in an Axisymmetric Laminar Diffusion Flame," *Twenty-Sixth Symposium (International) on Combustion*, The Combustion Institute, Pittsburgh, 1996, p. 2161-2170.

Sunderland, P.B., and Faeth, G.M., "Soot Formation in Hydrocarbon/Air Laminar Jet Diffusion Flames," *Combust. Flame*, **105**, p. 132 (1996).

Vandsburger, U., Kennedy, I.M., and Glassman, I., "Sooting Counter-Flow Diffusion Flames with Varying Velocity Gradients," *Twentieth Symposium (International) on Combustion*, The Combustion Institute, Pittsburgh, 1984, p. 1105.

Vandsburger, U., Kennedy, I., and Glassman, I., "Sooting Counterflow Diffusion Flames with Varying Oxygen Index," *Combust. Sci. Tech.*, **39**, p. 263 (1984).

Xu, Y., Smooke, M.D., Lin, P. and Long, M.B., "Primitive Variable Modeling of Multidimensional Laminar Flames," *Combust. Sci. Tech.*, **90**, p. 289 (1993).

Figure Captions

Figure 1 Schematic of the burner configuration.

Figure 2 Computed and measured temperature profiles at various heights in the flame.

Figure 3 Computed and measured methane profiles at various heights in the flame.

Figure 4 Computed and measured acetylene profiles at various heights in the flame.

Figure 5 Computed and measured benzene profiles at various heights in the flame.

Figure 6 Computed and measured soot volume fraction profiles at various heights in the flame.

Figure 7a Temperature isotherms of the computational model as a function of the radial and axial coordinates.

Figure 7b Methane isopleths (mole fractions) of the computational model as a function of the radial and axial coordinates.

Figure 7c Acetylene isopleths (mole fractions) of the computational model as a function of the radial and axial coordinates.

Figure 7d Benzene isopleths (mole fractions) of the computational model as a function of the radial and axial coordinates.

Figure 8a Soot volume fraction isopleths of the computational model as a function of the radial and axial coordinates.

Figure 8b Net soot production isopleths of the computational model as a function of the radial and axial coordinates.

Figure 8c Soot inception due to acetylene as a function of the radial and axial coordinates (rate of equation 2.1).

Figure 8d Soot oxidation due to OH as a function of the radial and axial coordinates (larger negative values imply higher oxidation rates).

Figure 9 Profiles of the ratio of the OH mole fraction to the equilibrium levels as a function of the radial coordinate at $z = 4.01$ cm.

Figure 10a-d Soot mass fraction isopleths for size classes 7-10. The sectional mass boundaries (min=127.0, max=1.5×10^{10}) have been placed linearly on a logarithmic scale. Peak soot mass concentration occurs in size class nine, whose mass-weighted mean diameter is about 48 nm (see Figure 11 for the mass boundaries of each class).

Figure 11a Contributions of the soot mass classes to the total soot volume fraction at z=1.0 cm.

Figure 11b Contributions of the soot mass classes to the total soot volume fraction at z=3.0 cm.

Figure 12a Soot volume fraction isopleths of the Fairweather *et al.* (1992) model as a function of the radial and axial coordinates.

Figure 12b Net soot production isopleths of the Fairweather *et al.* (1992) model as a function of the radial and axial coordinates.

Figure 12c Soot inception isopleths of the Fairweather *et al.* (1992) model as a function of the radial and axial coordinates.

Figure 12d Soot oxidation due to OH as a function of the radial and axial coordinates for the Fairweather *et al.* (1992) model (larger negative values imply higher oxidation rates).

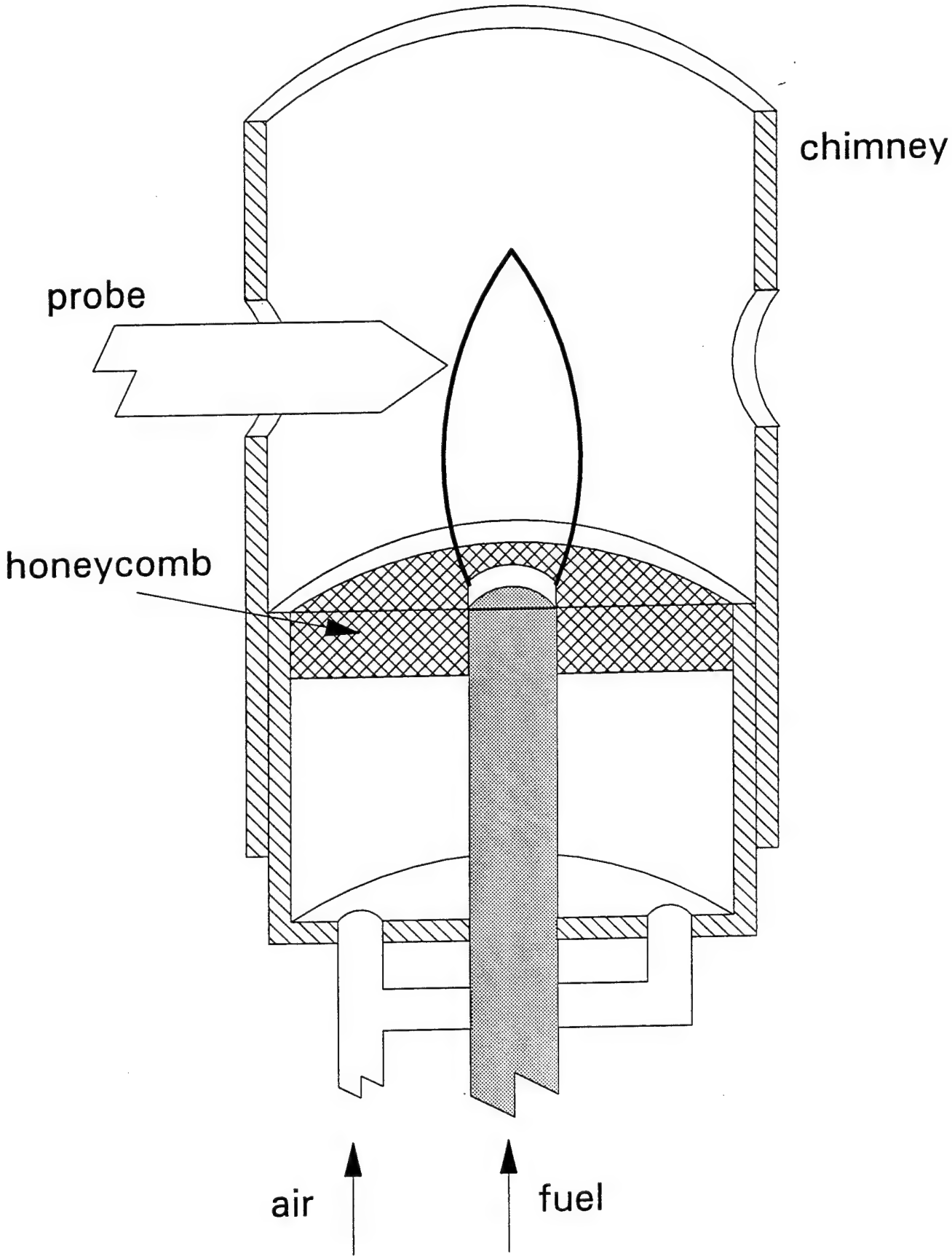

Figure 1

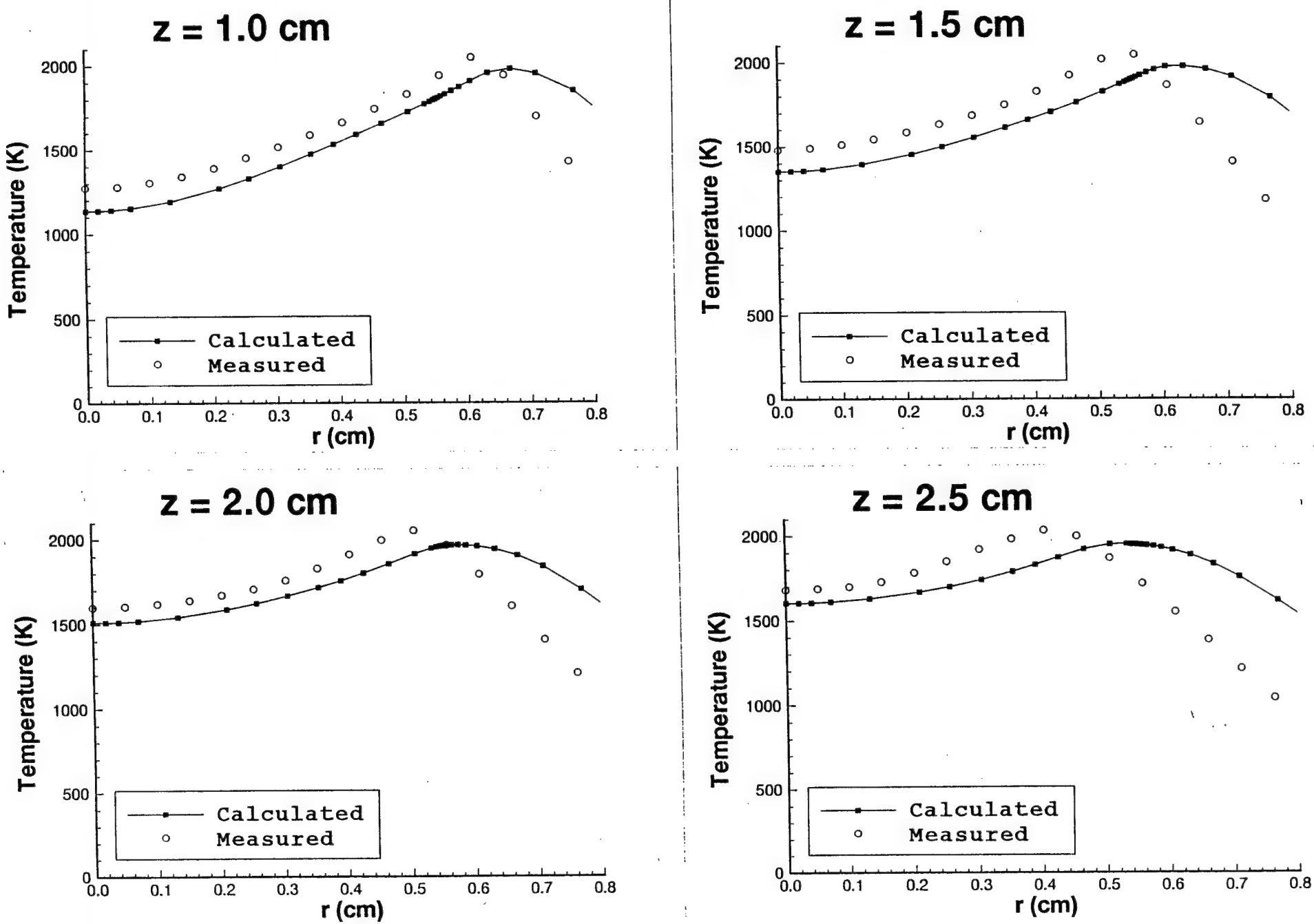
z = 1.0 cm
z = 1.5 cm
z = 2.0 cm
z = 2.5 cm
Temperature (K)
r (cm)
Calculated
Measured
0
500
1000
1500
2000
0.0
0.1
0.2
0.3
0.4
0.5
0.6
0.7
0.8

Figure 2

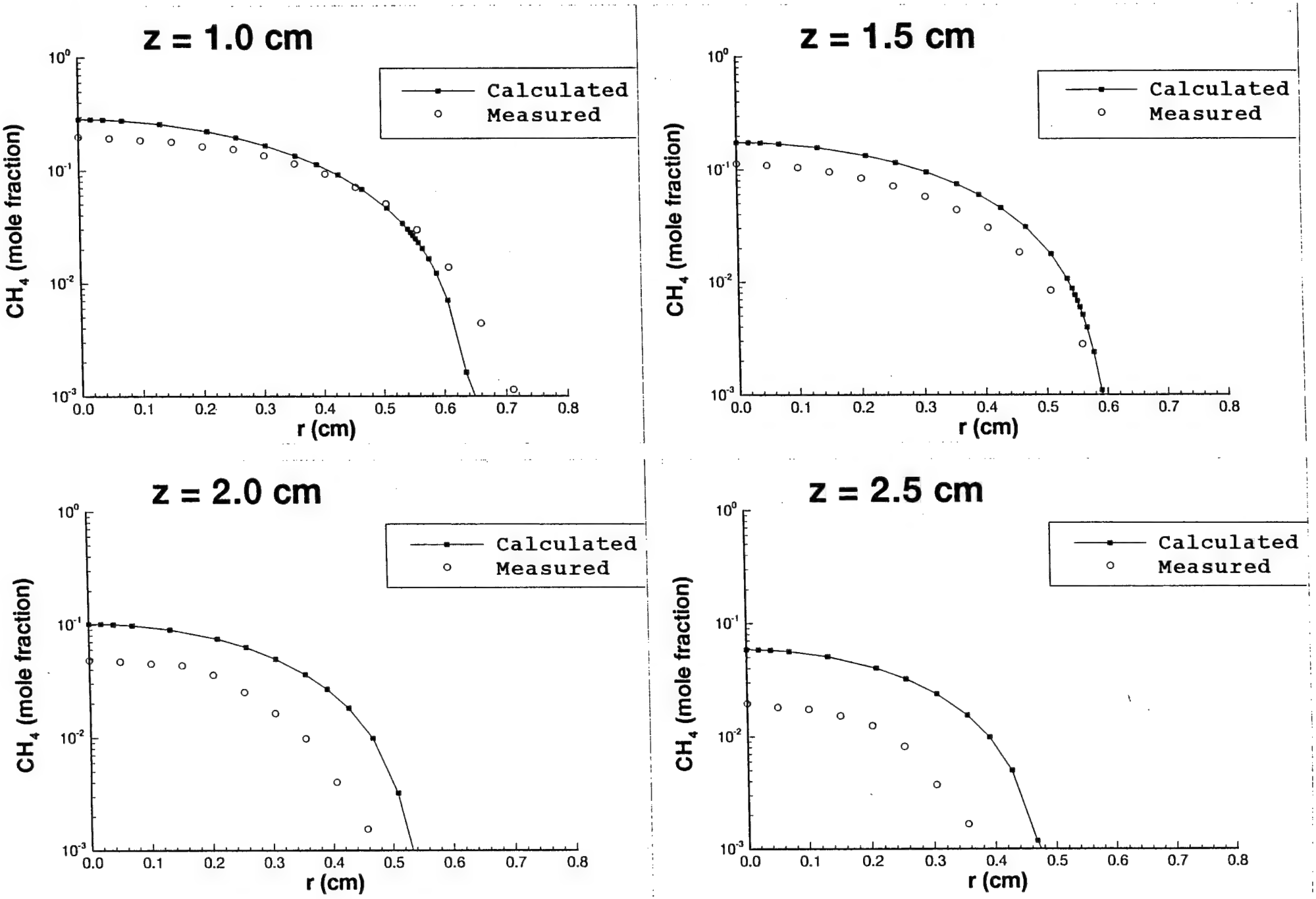
z = 1.0 cm
z = 1.5 cm
z = 2.0 cm
z = 2.5 cm
Calculated
Measured
CH4 (mole fraction)
r (cm)
10^0
10^-1
10^-2
10^-3
0.0
0.1
0.2
0.3
0.4
0.5
0.6
0.7
0.8

Figure 3

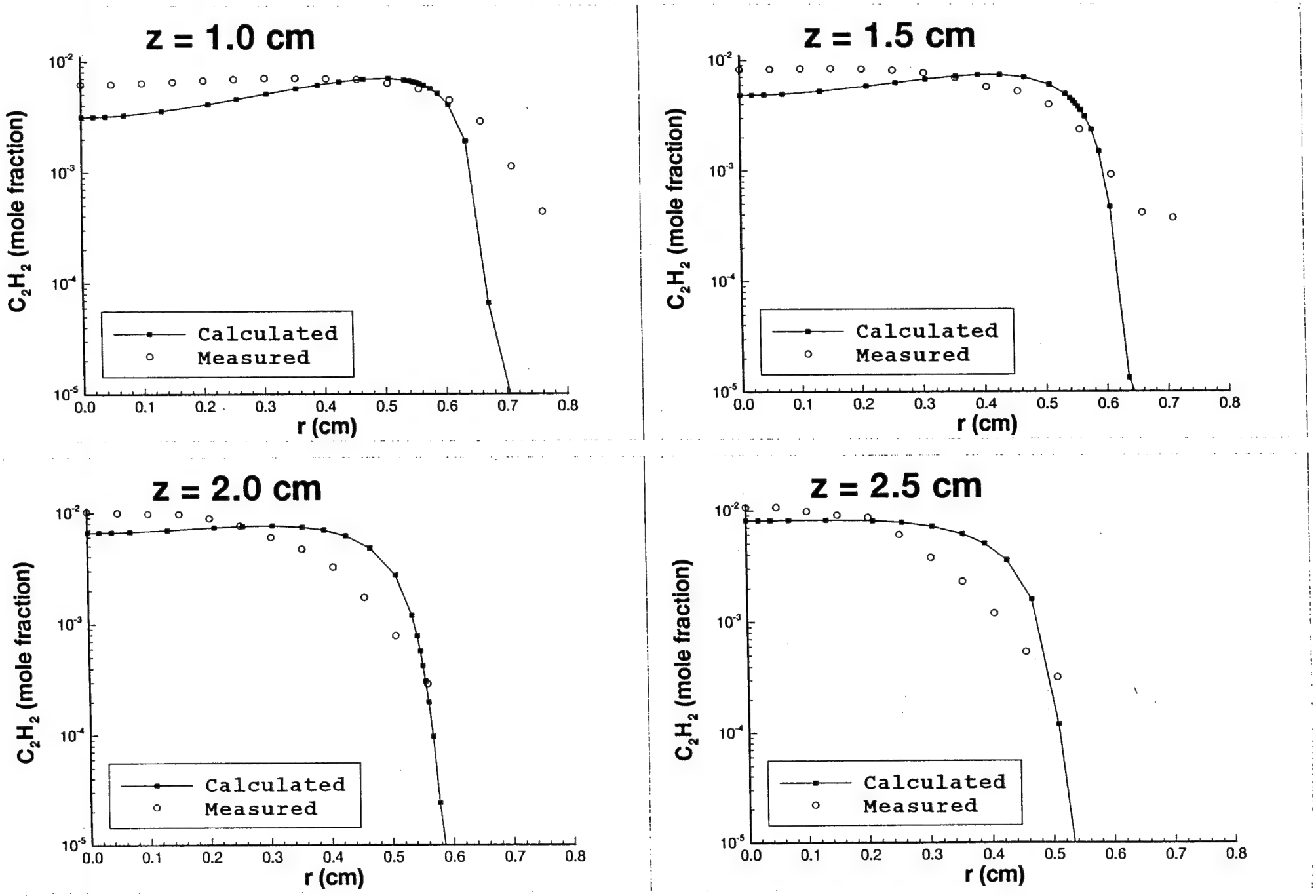
z = 1.0 cm
z = 1.5 cm
z = 2.0 cm
z = 2.5 cm
C_2H_2 (mole fraction)
r (cm)
Calculated
Measured
10^{-2}
10^{-3}
10^{-4}
10^{-5}
0.0
0.1
0.2
0.3
0.4
0.5
0.6
0.7
0.8

Figure 4

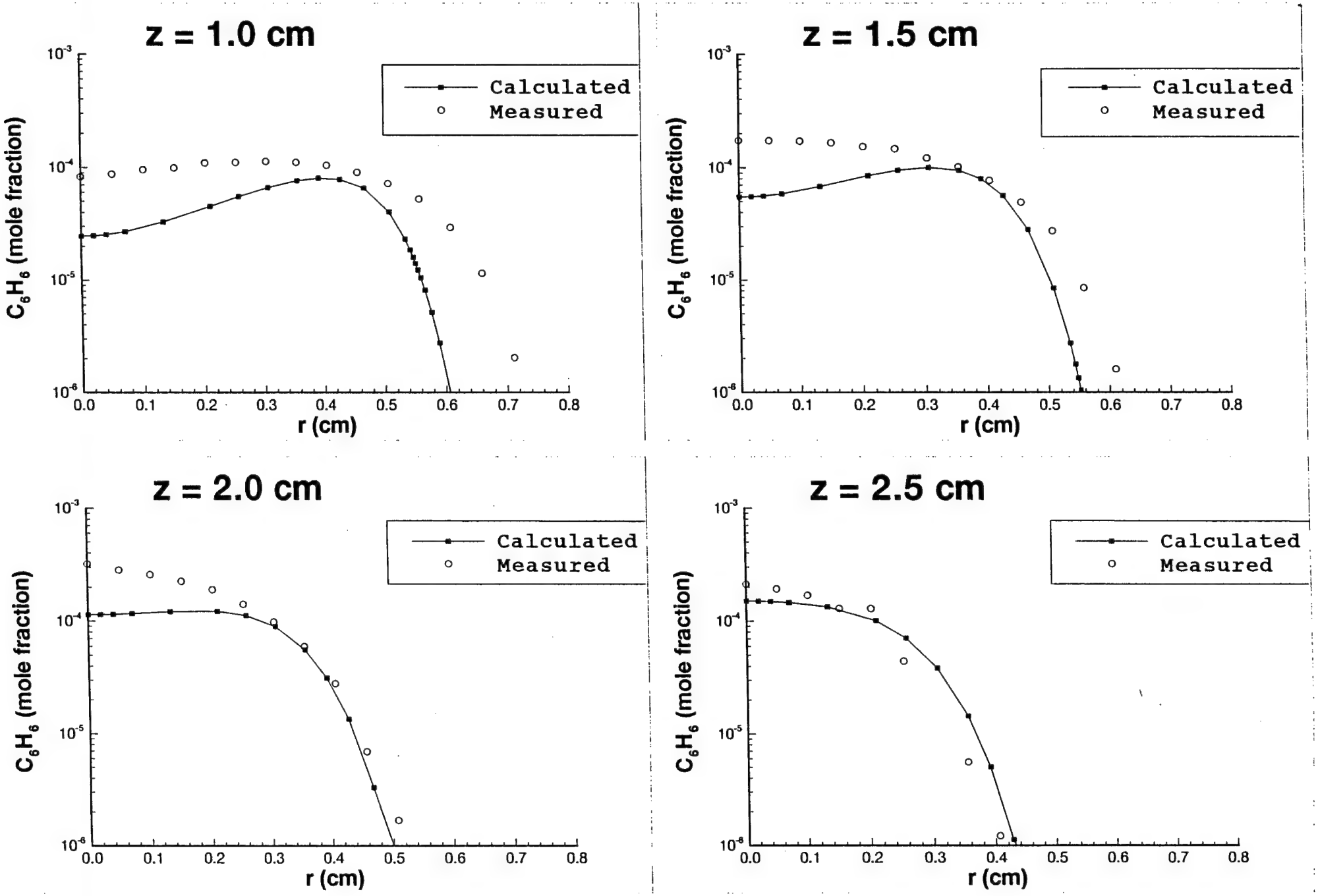
z = 1.0 cm
z = 1.5 cm
z = 2.0 cm
z = 2.5 cm
Calculated
Measured
C_6H_6 (mole fraction)
r (cm)
10^{-3}
10^{-4}
10^{-5}
10^{-6}
0.0
0.1
0.2
0.3
0.4
0.5
0.6
0.7
0.8

Figure 5

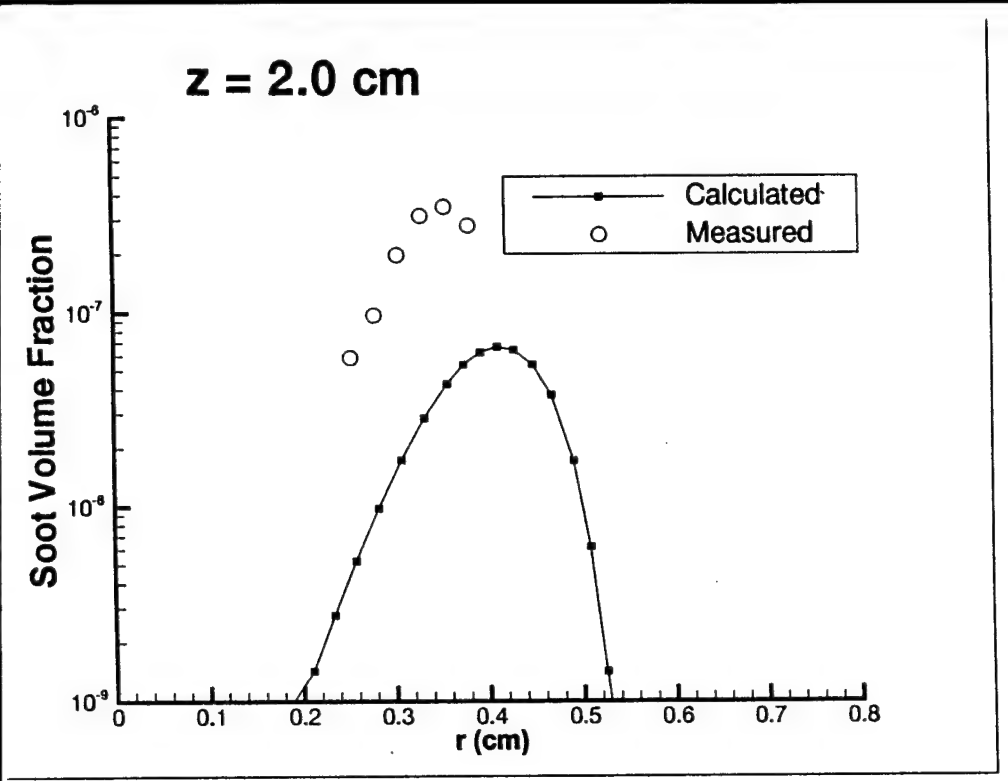
z = 2.0 cm
Soot Volume Fraction
r (cm)
Calculated
Measured

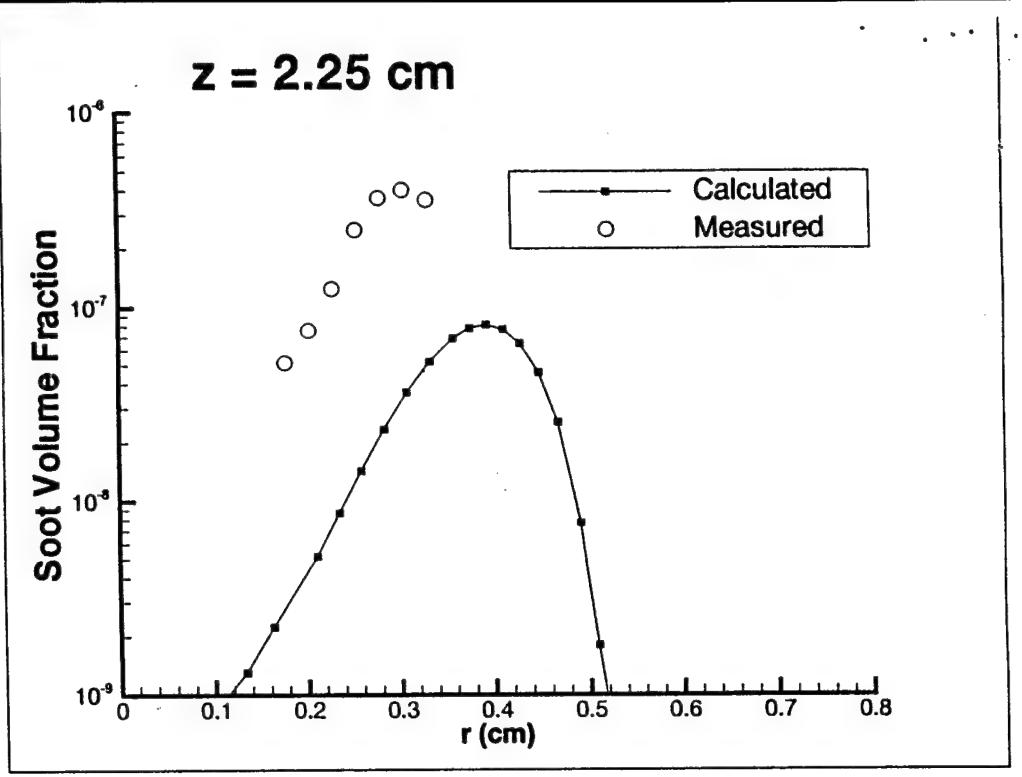
z = 2.25 cm
Soot Volume Fraction
r (cm)
Calculated
Measured

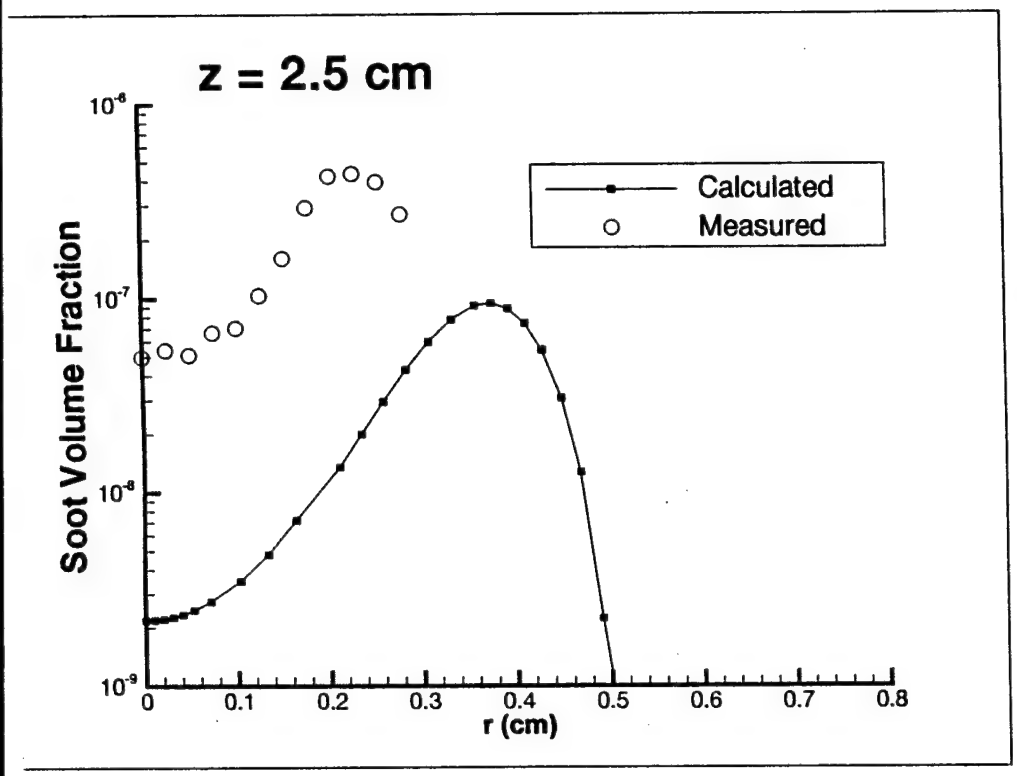
z = 2.5 cm
Soot Volume Fraction
r (cm)
Calculated
Measured

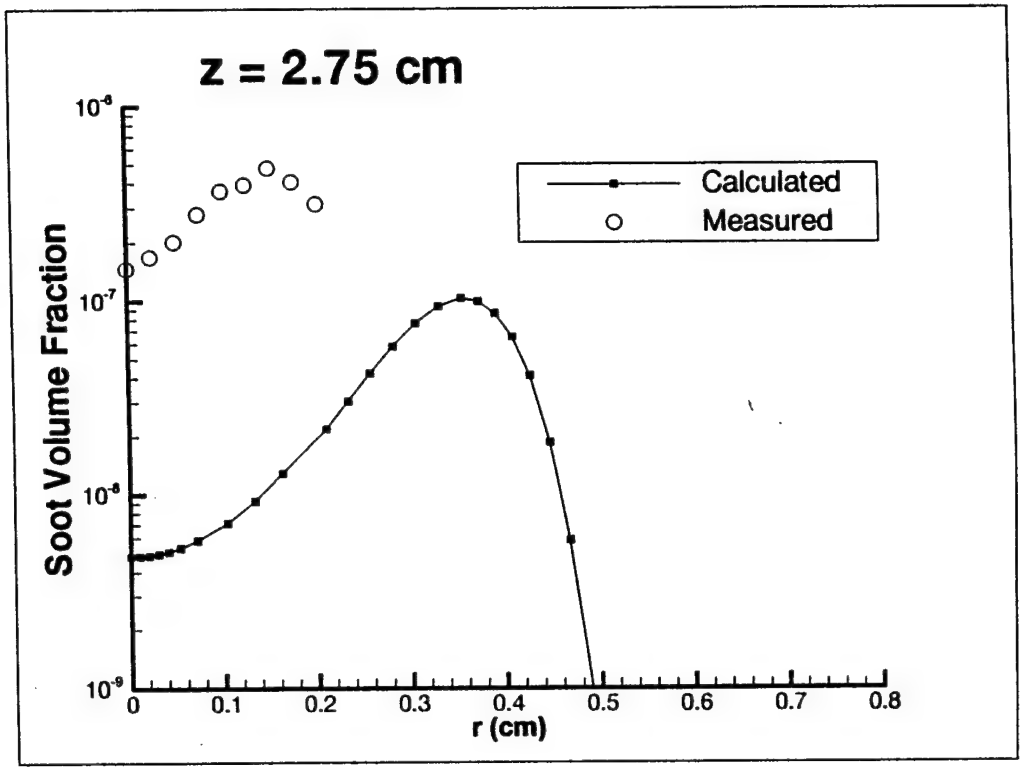
z = 2.75 cm
Soot Volume Fraction
r (cm)
Calculated
Measured

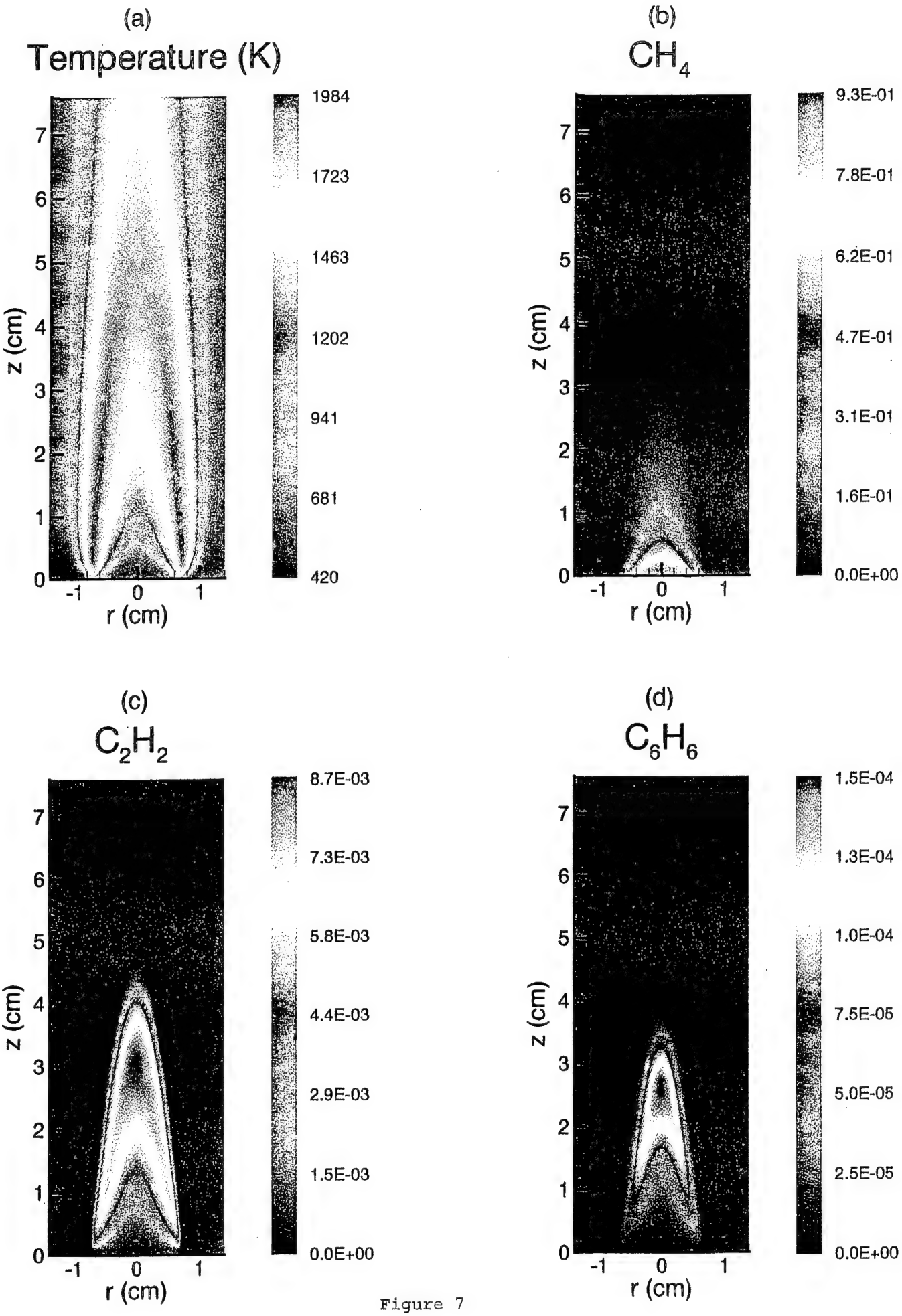
(a)
Temperature (K)
1984
1723
1463
1202
941
681
420
z (cm)
r (cm)
(b)
CH4
9.3E-01
7.8E-01
6.2E-01
4.7E-01
3.1E-01
1.6E-01
0.0E+00
z (cm)
r (cm)
(c)
C2H2
8.7E-03
7.3E-03
5.8E-03
4.4E-03
2.9E-03
1.5E-03
0.0E+00
z (cm)
r (cm)
(d)
C6H6
1.5E-04
1.3E-04
1.0E-04
7.5E-05
5.0E-05
2.5E-05
0.0E+00
z (cm)
r (cm)

Figure 7

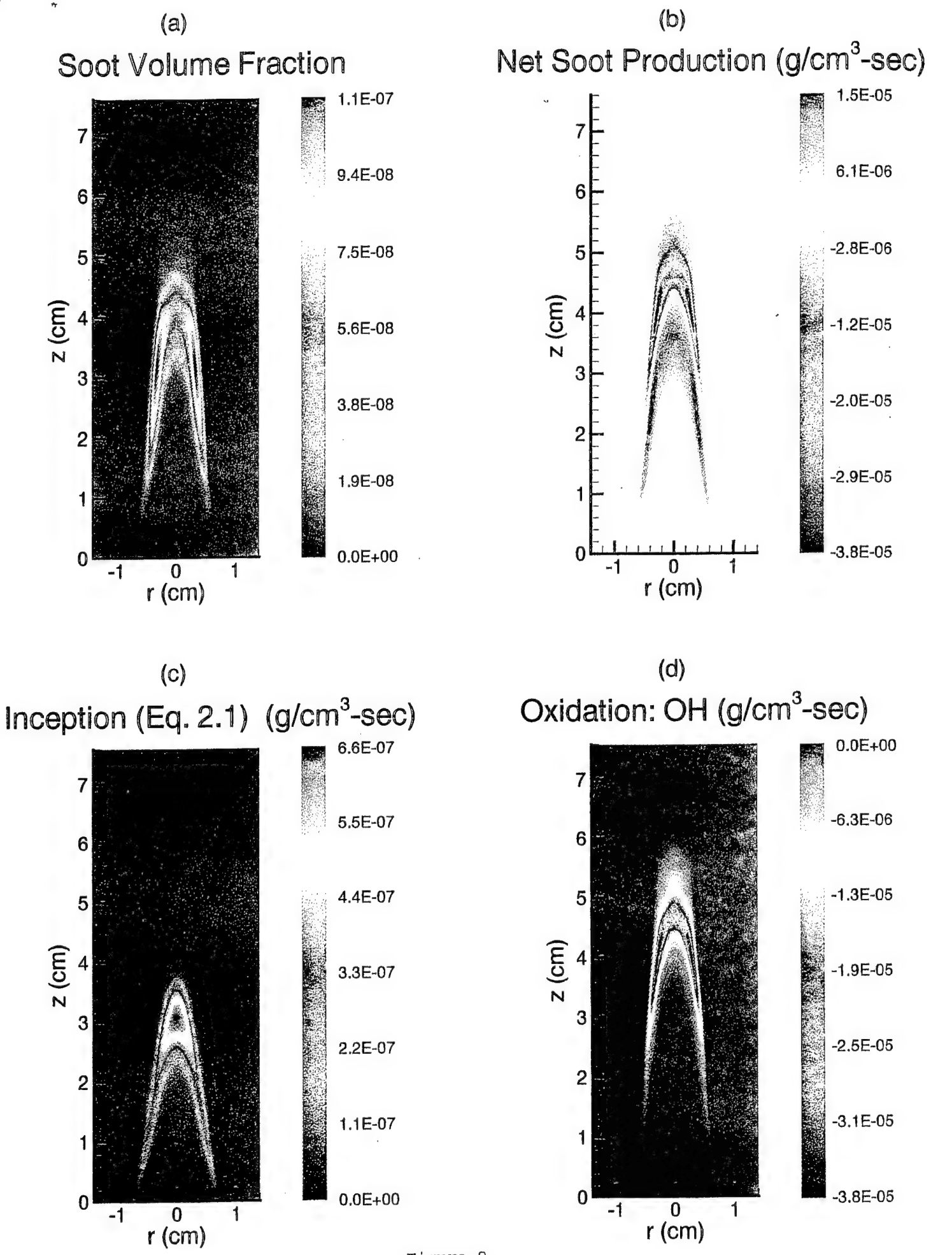
(a)
Soot Volume Fraction
1.1E-07
9.4E-08
7.5E-08
5.6E-08
3.8E-08
1.9E-08
0.0E+00
z (cm)
r (cm)
(b)
Net Soot Production (g/cm3-sec)
1.5E-05
6.1E-06
-2.8E-06
-1.2E-05
-2.0E-05
-2.9E-05
-3.8E-05
z (cm)
r (cm)
(c)
Inception (Eq. 2.1) (g/cm3-sec)
6.6E-07
5.5E-07
4.4E-07
3.3E-07
2.2E-07
1.1E-07
0.0E+00
z (cm)
r (cm)
(d)
Oxidation: OH (g/cm3-sec)
0.0E+00
-6.3E-06
-1.3E-05
-1.9E-05
-2.5E-05
-3.1E-05
-3.8E-05
z (cm)
r (cm)

Figure 8

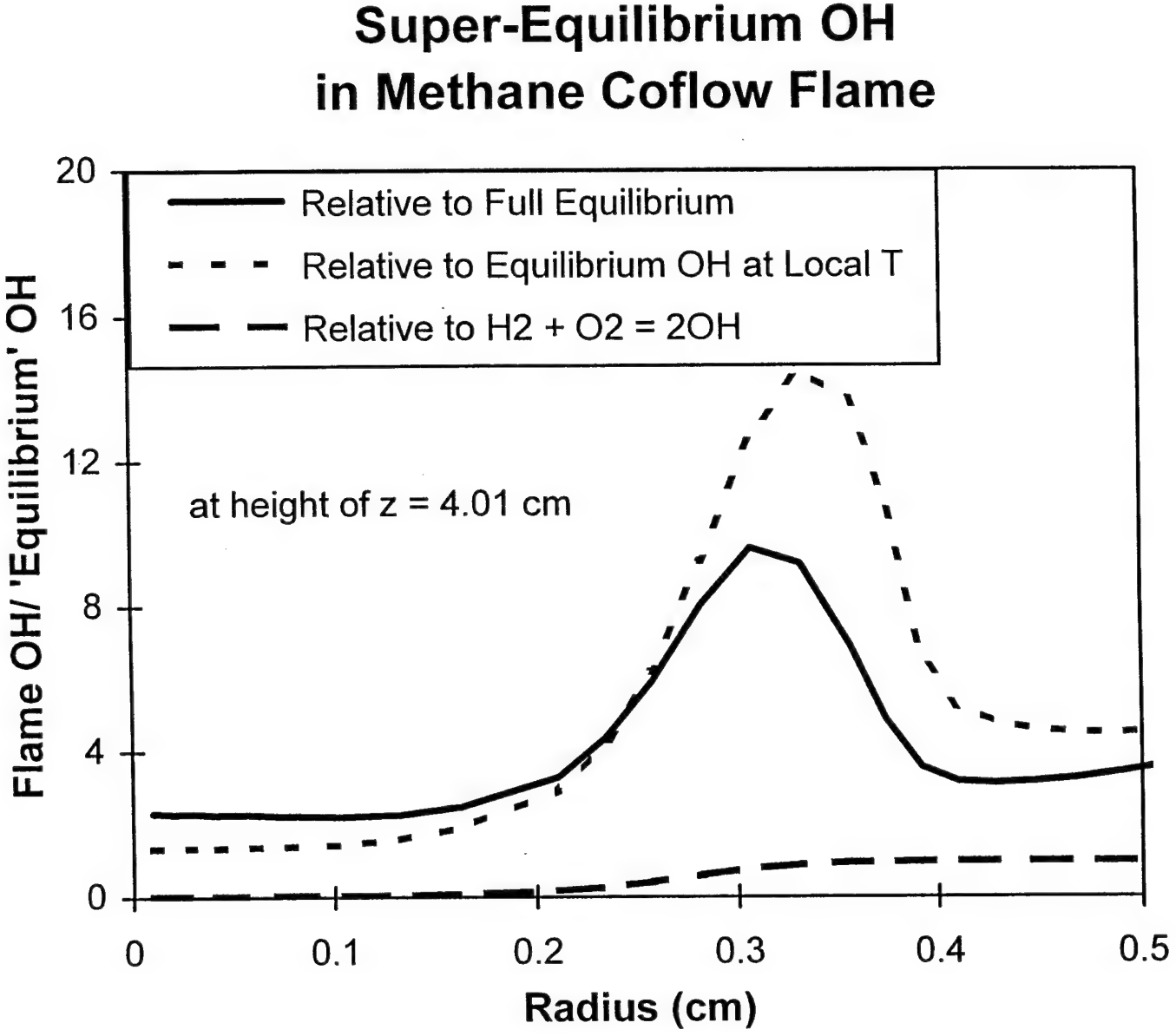
Super-Equilibrium OH
in Methane Coflow Flame
Relative to Full Equilibrium
Relative to Equilibrium OH at Local T
Relative to H2 + O2 = 2OH
at height of z = 4.01 cm
Flame OH/ 'Equilibrium' OH
20
16
12
8
4
0
0
0.1
0.2
0.3
0.4
0.5
Radius (cm)

Figure 9

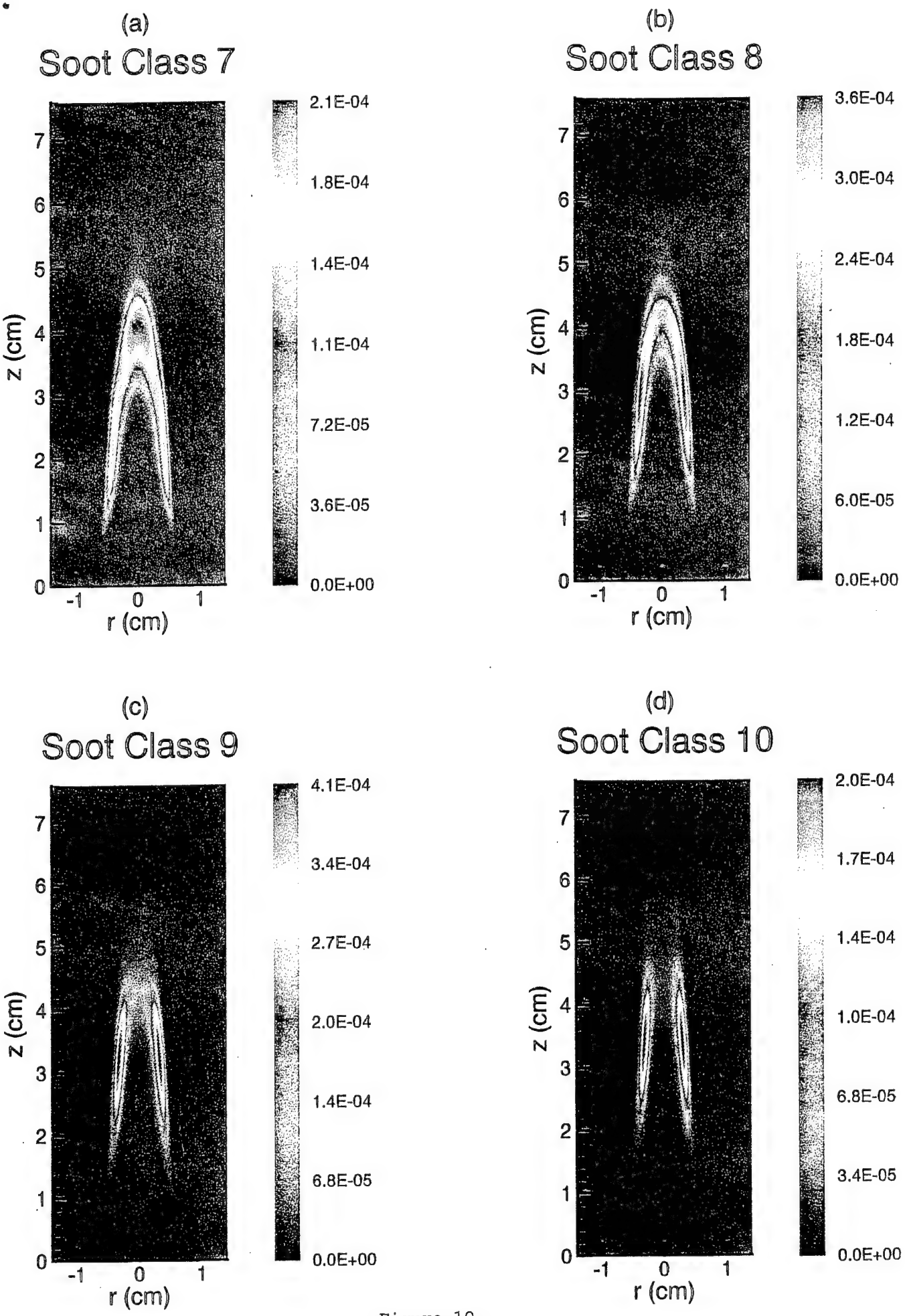
(a)
Soot Class 7
2.1E-04
1.8E-04
1.4E-04
1.1E-04
7.2E-05
3.6E-05
0.0E+00
z (cm)
r (cm)
(b)
Soot Class 8
3.6E-04
3.0E-04
2.4E-04
1.8E-04
1.2E-04
6.0E-05
0.0E+00
z (cm)
r (cm)
(c)
Soot Class 9
4.1E-04
3.4E-04
2.7E-04
2.0E-04
1.4E-04
6.8E-05
0.0E+00
z (cm)
r (cm)
(d)
Soot Class 10
2.0E-04
1.7E-04
1.4E-04
1.0E-04
6.8E-05
3.4E-05
0.0E+00
z (cm)
r (cm)

Figure 10

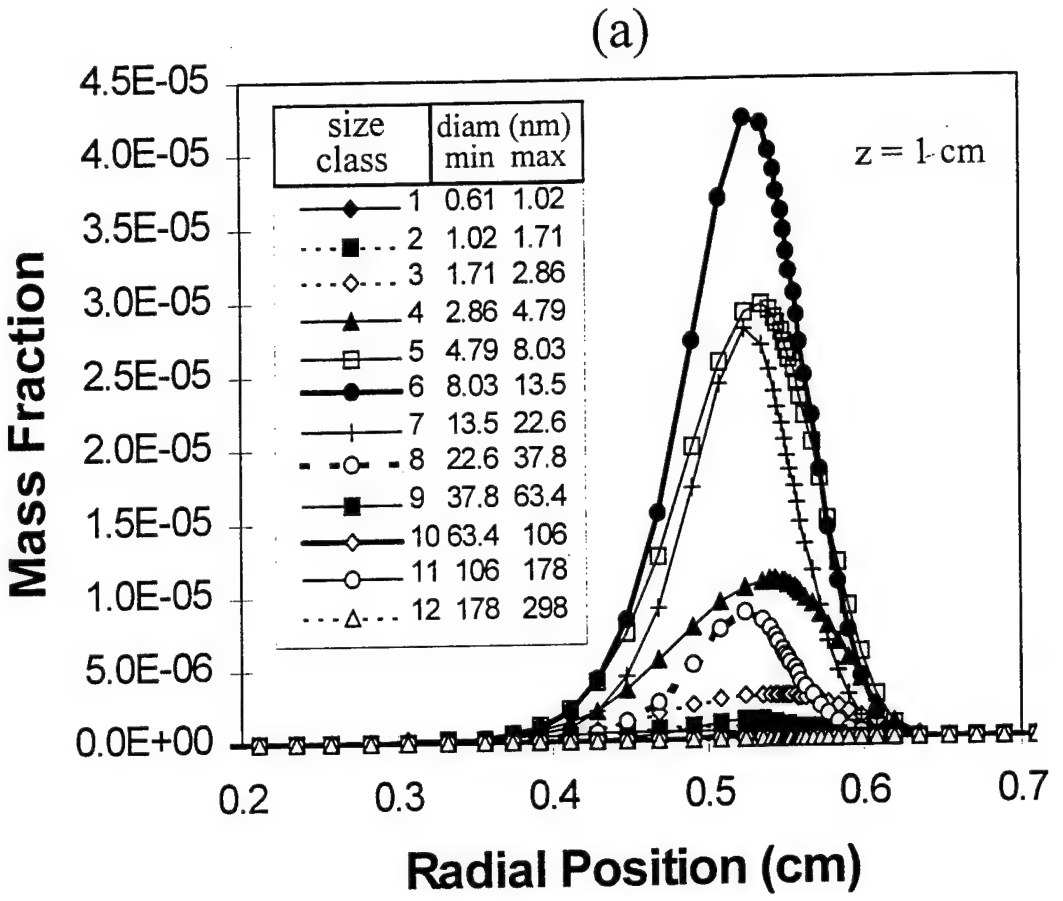
(a)
Mass Fraction
4.5E-05
4.0E-05
3.5E-05
3.0E-05
2.5E-05
2.0E-05
1.5E-05
1.0E-05
5.0E-06
0.0E+00
size class
diam (nm) min max
1 0.61 1.02
2 1.02 1.71
3 1.71 2.86
4 2.86 4.79
5 4.79 8.03
6 8.03 13.5
7 13.5 22.6
8 22.6 37.8
9 37.8 63.4
10 63.4 106
11 106 178
12 178 298
z = 1 cm
0.2
0.3
0.4
0.5
0.6
0.7
Radial Position (cm)

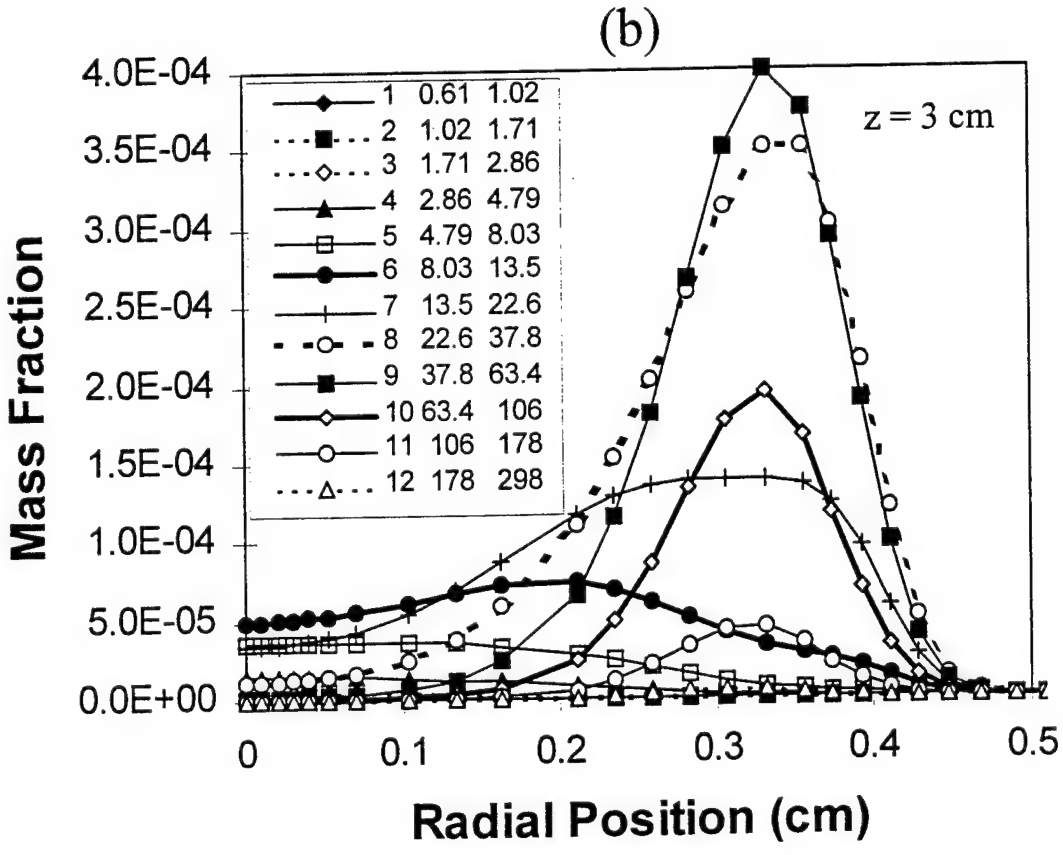
(b)
Mass Fraction
4.0E-04
3.5E-04
3.0E-04
2.5E-04
2.0E-04
1.5E-04
1.0E-04
5.0E-05
0.0E+00
1 0.61 1.02
2 1.02 1.71
3 1.71 2.86
4 2.86 4.79
5 4.79 8.03
6 8.03 13.5
7 13.5 22.6
8 22.6 37.8
9 37.8 63.4
10 63.4 106
11 106 178
12 178 298
z = 3 cm
0
0.1
0.2
0.3
0.4
0.5
Radial Position (cm)

Figure 11

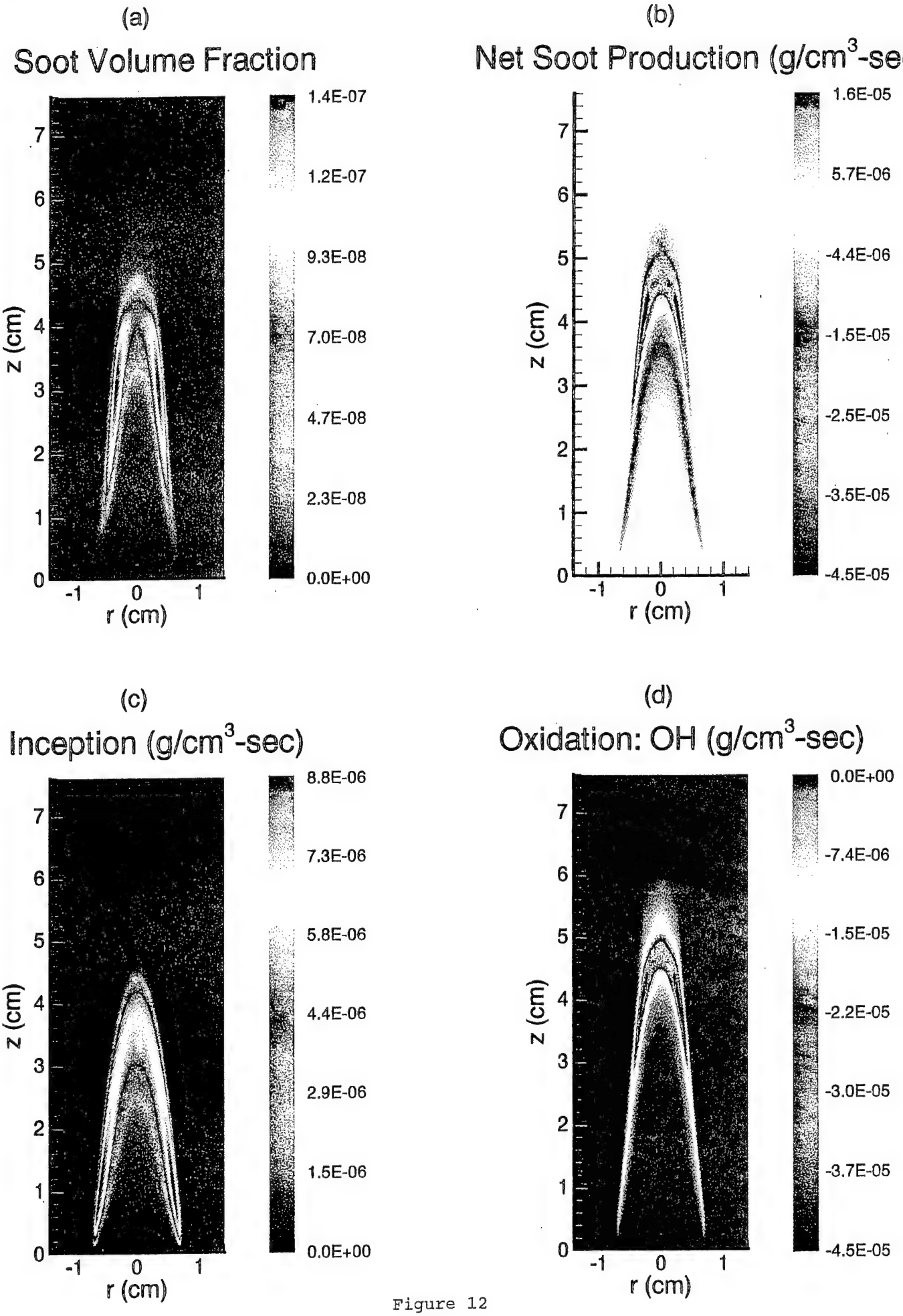
(a)
Soot Volume Fraction
1.4E-07
1.2E-07
9.3E-08
7.0E-08
4.7E-08
2.3E-08
0.0E+00
z (cm)
r (cm)
(b)
Net Soot Production (g/cm3-sec)
1.6E-05
5.7E-06
-4.4E-06
-1.5E-05
-2.5E-05
-3.5E-05
-4.5E-05
z (cm)
r (cm)
(c)
Inception (g/cm3-sec)
8.8E-06
7.3E-06
5.8E-06
4.4E-06
2.9E-06
1.5E-06
0.0E+00
z (cm)
r (cm)
(d)
Oxidation: OH (g/cm3-sec)
0.0E+00
-7.4E-06
-1.5E-05
-2.2E-05
-3.0E-05
-3.7E-05
-4.5E-05
z (cm)
r (cm)

Figure 12

Appendix B
Computational and Experimental Study of Soot Formation in a Coflow, Laminar Diffusion Flame

COMPUTATIONAL AND EXPERIMENTAL STUDY OF SOOT FORMATION IN A COFLOW, LAMINAR ETHYLENE DIFFUSION FLAME

C. S. McEnally[1], A. M. Schaffer[1], M. B. Long[1], L. D. Pfefferle[1] and M. D. Smooke[1]
M. B. Colket[2] and R. J. Hall[2]

[1] *Yale Center for Combustion Studies, Yale University, New Haven, CT 06520-8284, USA.*

[2] *United Technologies Research Center, East Hartford, CT 06108, USA.*

Corresponding Author: Prof. M.D. Smooke
Department of Mechanical Engineering
Yale University
PO BOX 208284
New Haven, CT 06520–8284, USA
phone: (203) 432 4344
FAX: (203) 432 6775
e-mail: *smooke%smooke@biomed.med.yale.edu*

Colloquium Topic: Soot, PAH and Air Toxics

COMPUTATIONAL AND EXPERIMENTAL STUDY OF SOOT FORMATION IN A COFLOW, LAMINAR ETHYLENE DIFFUSION FLAME

Abstract

A sooting, ethylene coflow diffusion flame has been studied both experimentally and computationally. The fuel is diluted with nitrogen and the flame is slightly lifted to minimize the effects of the burner. Both probe (thermocouple and gas-sampling techniques) and optical diagnostic methods (Rayleigh scattering and laser-induced incandescence) are used to measure the temperature, gas species and soot volume fractions. A detailed soot growth model in which the equations for particle production are coupled to the flow and gaseous species conservation equations has been used to investigate soot formation in the flame. The two-dimensional system couples detailed transport and finite rate chemistry in the gas phase with the aerosol equations in the sectional representation. The formulation includes detailed treatment of the transport, inception, surface growth, oxidation, and coalescence of soot particulates. Effects of thermal radiation and particle scrubbing of gas phase growth and oxidation species are also included. Predictions and measurements of temperature, soot volume fractions and selected species are compared over a range of heights and as a function of radius. The formation of benzene is primarily controlled by the recombination of propargyl radicals and benzene production rates are found to limit the rate of inception as well as the net rate of soot growth. The model predicted soot volume fractions well along the wings of the flame, but underpredicted soot volume fractions by a factor of four along the centerline. Oxidation of particulates is dominated by reactions with hydroxyl radicals which attain levels approximately ten times higher than calculated equilibrium levels. Gas cooling effects due to radiative loss are shown to have a very significant effect on predicted temperatures.

COMPUTATIONAL AND EXPERIMENTAL STUDY OF SOOT FORMATION IN A COFLOW, LAMINAR ETHYLENE DIFFUSION FLAME

Introduction

Combustion-generated soot particulates from land-based sources pose a significant health risk and are the subject of stringent new EPA regulations. Now, soot emissions from aircraft face the likelihood of tightened regulation. Besides regulatory issues, soot contributes to thermal radiation loads on combustor liners and turbine blades. Soot emissions enhance contrail formation and tactical visibility of military aircraft. Further, impaction of soot on low observable surfaces can compromise the radar signature of aircraft. Quantitative understanding of the soot growth and oxidation mechanisms and the ability to model accurately these processes may be critical to the development of strategies to control emissions.

Despite the complexities of modeling soot formation in flames using detailed chemistry, the linkage of soot production to radiation and bulk flame properties is so strong that the coupled treatment of this problem is becoming a necessity for quantitative modeling of flame structure. Such modeling for a generic multidimensional configuration is still beyond our current computational ability. The laminar diffusion flame, however, provides an environment to investigate the interaction of soot formation with detailed gas-phase chemistry in a multidimensional system.

Recent investigators [1,2] have modeled jet diffusion flames, using simplified, monodisperse soot formation models with skeletal kinetic mechanisms. We recently modified the sectional soot formation model developed in [3,4] for incorporation into a code for a laminar axisymmetric diffusion flame (cylindrical fuel jet surrounded by a coflowing oxidizer) [5]. This model employs a velocity-vorticity formulation [6] in which the governing conservation equations are solved with detailed transport and finite rate chemistry submodels to predict the temperature, species mass fractions and velocity fields as functions of the two independent coordinates. When this model was applied to a sooting methane-air flame, comparisons between the model and experiments were reasonable, yet the matching of bulk flame properties was insufficient to enable quantitative comparison of the calculated and measured soot profiles. In contrast to these results was the nearly perfect agreement obtained between the model and optical diagnostics of temperature, fuel and NO for a non-sooting, methane coflow diffusion flame [7]. This latter blue flame was diluted and lifted far from the burner inlet. A speculated problem in the sooting flame which was attached to the burner was uncertain inlet boundary conditions due to preheating of the fuel and air.

The purpose of the present investigation is to study a coflow diffusion flame, but partially lifted, to minimize effects of uncertain inlet conditions and to compare results from calculations, intrusive diagnostics and non-intrusive diagnostics to determine the strengths and weaknesses of each approach. Through this study, it is expected that flame types, amenable to modeling, and correspondingly appropriate diagnostic methods can

be recommended for future studies. Furthermore, this study should provide additional information on the nature of soot formation and growth in coflow diffusion flames.

Problem Formulation

Soot Modeling

Soot kinetics are modeled as coalescing, solid carbon spheroids undergoing surface growth in the free molecule limit. The particle mass range of interest is divided into sections [8] and an equation is written for each section including coalescence, surface growth, and oxidation. Sectional analysis makes it possible to obtain the particle size distribution without a-priori assumptions about the form of the distribution. For the smallest section, an inception source term is included. The transport conservation equation for each section includes thermophoresis, an effective bin diffusion rate, and source terms for gas-phase scrubbing. The gas and soot equations are additionally coupled through non-adiabatic radiative loss in the optically-thin approximation. The inception model employed here is based on an estimate of the formation rate of two- and three-ringed aromatic species (naphthalene and phenanthrene), and is a function of local acetylene, benzene, phenyl and molecular hydrogen concentrations [5]. The contributions from the inception processes are incorporated in the first sectional bin, whose lower mass boundary is set equal to the mass of the smallest inception species. In the sectional representation [8], the sectional mass boundaries vary linearly on a logarithmic scale. The number of sections required for convergence must be examined for each problem and depends on the relative magnitudes of surface growth and inception. Oxidation of soot by O_2 and OH is treated as described in [4]. The surface growth rate is based upon that of Harris and Weiner [9] with a nominal activation energy of 31.8 kcal/mole as suggested by Hura and Glassman [10]. We empirically adjusted the Harris and Weiner rate by a factor of two as in [5].

Governing Equations and Numerical Method

The axisymmetric computational model employs the gas-phase diffusion flame equations in the velocity-vorticity formulation [6] with the sectional approach presented in [4]. Buoyancy is included in the model. The result is a strongly coupled set of elliptic partial differential equations. We solve for the radial and axial velocities, the vorticity, the temperature, the gas phase species and the particle sectional mass fractions. The system is closed with the ideal gas law and appropriate boundary conditions are applied on each side of the computational domain. Local properties are evaluated using vectorized and highly optimized transport and chemistry libraries [11]. The sectional thermophoretic velocities in the free molecule regime are given in [3] as are the sectional diffusion velocities which are written with a mass weighted mean diffusion coefficient for each size class. In the optically-thin radiation model used in our calculations the significant radiating species, in addition to particulates, are H_2O, CO and CO_2. Given the length scales of the flame investigated, it is highly unlikely that self-absorption is important. Although the soot volume fraction reaches near ppm levels, the narrowness of the soot shell (1-2 mm) will mitigate any self absorption effects.

The governing conservation equations are solved on a two-dimensional mesh by combining a steady-state and a time-dependent solution method [7]. A time-dependent approach

is used to help obtain a converged numerical solution on an initial coarse grid. Grid points are then inserted adaptively and Newton's method is used to complete the problem.

Experimental Methods

Atmospheric pressure, overventilated, axisymmetric, coflowing, nonpremixed laminar flames were generated with a burner in which the fuel flows from an uncooled 4.0 mm inner diameter vertical brass tube (wall thickness 0.038 mm) and the oxidizer flows from the annular region between this tube and a 50 mm diameter concentric tube (see Figure 1). The oxidizer was air while the fuel was a mixture containing ethylene and nitrogen. Fuel flowrates were governed by electronic mass flow controllers accurate to within 5%. The same burner apparatus was used for all the experiments. The temperature of the brass tube for this slightly lifted flame was less than 330 K.

Probe Measurements

The probe measurement procedures have been described previously [12,13]. Gas temperatures were measured with 75 μm wire-diameter Type R thermocouples and corrected for radiation heat transfer effects using standard techniques [12]. A rapid insertion procedure was used to minimize errors due to soot deposition onto the thermocouple. In soot-free regions, the absolute uncertainty of these measurements is estimated to be $\pm$50 K and the relative uncertainty to be $\pm$10 K.

Soot concentrations were measured with the same thermocouples using thermocouple particle densitometry (TPD), a technique in which soot volume fraction is inferred from measured rates of soot particle mass transfer to the thermocouple junction [12]. The results have a relative uncertainty of 30%, and an absolute uncertainty of 50%.

Species concentrations were measured by extracting gas samples from the flames with a narrow-tipped quartz microprobe and analyzing these samples with on-line mass spectrometry [13]. Acetylene and ethylene were quantified with an Extrel C50 variable-ionization-energy electron-impact/quadrupole mass spectrometer, and C3 to C12 hydrocarbons with a custom-built photoionization/time-of-flight mass spectrometer. Measurements were directly calibrated and have an absolute uncertainty of 30%.

Profiles were generated by moving the burner with translation stages. The axial and radial coordinates, designated z and r, have a relative uncertainty of $\pm$0.2 mm and an absolute uncertainty of $\pm$0.5 mm.

Laser diagnostic measurements

Using planar laser imaging, we obtain two-dimensional fields of temperature, fuel concentration, and soot volume fraction in the C_2H_4/N_2 flame. The temperature field is determined using the two scalar approach of Stårner et al. [14] and included the measurement of Rayleigh scattering and the use of the computed fuel concentration.

The soot volume fraction field is determined by laser-induced incandescence (LII). At sufficient laser intensities, the LII signal has been shown to be directly proportional to soot volume fraction [15]. The probe measurements of the soot volume fraction are used for

calibration.

The second harmonic of an Nd:YAG laser (532 nm) is focused into a 18.0 mm tall vertical sheet over the center of the burner. The incandescence and scattered light is collected perpendicular to the laser axis. The light passes through an appropriate interference filter and then is focused onto an intensified CCD camera.

For Rayleigh scattering, images at two downstream locations are acquired. For the first set of images the laser sheet is 3 mm off the surface of the burner. A 532 nm interference filter (10 nm FWHM) is used to collect the Rayleigh scattering. In the region from 11.0-22.0 mm downstream, interference from LII and particle scattering dominate the Rayleigh signal which is not plotted in this region (see Figure 2). Rayleigh images are also acquired with the bottom edge of the laser sheet just above the flame tip (22 mm off the burner surface), where temperatures are just below adiabatic flame temperatures, and where there are no interferences from LII. Laser energy is set to 100 mJ/pulse.

With the laser sheet 8 mm off the burner surface, laser-induced incandescence images are acquired. A 450 nm (10 nm FWHM) interference filter is used to collect the incandescence signal. In the region of greatest incandescence signal a survey is conducted of incandescence signal versus laser intensity to maximize signal intensity without saturation (e.g., soot destruction) at any point in the flow field. All images are corrected for optical throughput, background scattering signals and non-uniformities in beam profile. Images are also corrected for flame luminosity and non-uniform detector response.

Results

The chemical kinetic mechanism for ethylene combustion has 45 species and 233 reactions. It was derived from GRIMech 1.2 [16], based upon comparisons to experimental data on ethylene from perfectly stirred and flow reactors and ignition delay data. It includes reactions describing the formation and oxidation of benzene, and related species.

Fuel and nitrogen are introduced through the center tube (4mm id) utilizing a parabolic velocity profile and air through the outer coflow with a plug flow profile. Both velocity profiles were those employed in the experiments. The mass fractions at the burner exit are 0.32 and 0.68 for ethylene and nitrogen, respectively and the bulk averaged velocity is 35 cm/sec. The coflow air velocity was 35 cm/sec. Reactant temperatures were assumed to be 298 K. All radial velocities were assigned to zero at the flame base.

Calculations were performed on an IBM RS/6000 Model 590 computer. In the computations presented, nine soot size classes were included in the model with approximately 10,000 adaptively refined grid points. Starting from a converged solution for an ethylene-air flame without the sectional equations, we typically obtained converged solutions for the complete gas-soot problem in several hours of computer time. The number of soot bins in these calculations was constrained by the maximum memory of our computer. Based upon the relative magnitudes of the inception and surface growth rates, we anticipate that the restricted number of bins has not caused significant numerical error.

In Figure 2, temperatures determined from the model, the thermocouple and Rayleigh

scattering are compared. Radial comparisons between the computations and thermocouple measurements at several axial locations are plotted in Figure 3. Agreement between the temperature computations and measurements is excellent throughout the flame. The peak temperatures were 1953 K for the computations and 2040 K for the thermocouple measurements. Peak Rayleigh temperatures were somewhat lower than the computations. With radiation from soot suppressed, the peak predicted temperature is 1990 K; with both gas band and soot radiation suppressed, the peak predicted temperature rises to 2061 K. Integration of the computed radiative dissipation over the flame volume yields a predicted radiative power that is about 12% of the total heat release. Flame height, as estimated by the attainment of the peak temperature on the centerline was 2.7 ($\pm$ 0.05) cm for all three cases. This agreement is dramatically better than that obtained in the attached methane-air diffusion flame [5] in which the experimental inlet conditions were not well defined. It also should be noted that the excellent agreement on the air-side of the flame contrasts with the results obtained in [5] where there was substantial difference between the measured and computed temperatures. The calculated rise in temperature along the centerline is delayed relative to the increase as determined from the probe measurements, but is in good agreement with the optical results. We speculate that accurate determination of temperatures in this region of the flame, where thermal gradients are very large, with a thermocouple is difficult due to conduction along the thermocouple wires.

Ethylene profiles were obtained from all three methods; two-dimensional contour plots and the radial profiles at various axial heights (not shown here) depict excellent agreement among the model and the Raman scattering experiments. Peak concentrations of acetylene, the principal carbon-containing species involved in surface growth, as calculated by the model and as determined by the probe measurements are 4.3% and 3.7%. Peak concentrations are located along the centerline about 15 mm above the burner lip and generally the profile shapes agree well, at least in regions of the flame which do not have other contributions to the mass 26 peak. Experimentally, acetylene decays a little faster along the centerline than does the model. Contours for benzene are shown in Figure 4. Peak predicted benzene mole fractions are 1.8×10^{-4} versus a peak experimental value of 1.6×10^{-4}. A reaction path analysis demonstrated that benzene was formed principally through propargyl recombination reactions (to form H + C_6H_5). Propargyl, in turn, is formed through the oxidation of diacetylene, i.e., C_4H_2 + OH $\rightarrow$ C_3H_2 + HCO followed by, C_3H_2 recombination with H atoms. When soot inception scrubbing of benzene is not activated in the model, the peak benzene concentration increases by a factor of 38%. This contrast demonstrates the importance of scrubbing effects and demonstrates how benzene levels are determined based upon a balance of its formation and its conversion to higher molecular weight hydrocarbon species. Other than the inception process, the principal loss mechanism for benzene in these fuel-rich, pyrolytic zones, is via the thermal decomposition of phenyl radical and such decomposition does not occur rapidly until the gas temperature exceeds 1800 K, a point after the bulk of soot inception and growth has occurred.

Soot volume fractions f_v, as determined from the model, thermophoretic sampling, and LII (calibrated based on probe measurements) are illustrated in Figure 5. Agreement between the two experimental techniques is considered very good. Peak soot f_v from the model agrees well with the experimental values; however, soot still peaks off the centerline in the wing region for the model and on the centerline for the two sets of experiments. Peak

values are 7.85×10^{-7} for the model and 1.0×10^{-6} for the thermophoretic measurements. When the predicted values ultimately peak along the centerline, they are a factor of four below the measured value. As illustrated, the thermophoretic sampling method detects soot particles closer to the burner than does LII. The sampling method has the ability to detect not only carbonized soot but any translucent particles as well. We also note in Figure 5 that the computations illustrate an extended wing region compared to that of both experimental methods. This is due, in part, to the fact that the soot volume fraction in the lower wing regions are below the lower detectivity limits of the experimental methods. In Figure 6 we compare computational and thermophoretic sampling soot volume fractions as a function of the radial coordinate at several axial heights. While the agreement at 18 mm is excellent, it is clear that the model does fall short in being able to predict soot values that are as large as those measured on the centerline. The tendency for soot to peak in the wings is typically observed in more heavily sooting flames [2]. Relative spatial distributions for the separate processes of surface growth, soot inception, and oxidation as determined from the model are illustrated in Figures 7, 8, and 9, respectively.

A brief analysis of these results indicates that the high soot oxidation rates observable in the wings of this flame are attributable to super-equilibrium OH concentrations, consistent with our previous study [5] and that of several previous investigations [17]. The lack of including the effects of superequilibrium OH in such coflow flames are likely to result in significant errors in the analysis/interpretations. Variations in the base soot model surface growth, inception, and oxidation rates were carried out to gain understanding of the possible causes of the difference between the model and the experiments. These studies did not yield a clean explanation of the discrepancies. We conclude that the ability to make quantitative soot predictions remains limited by some fundamental uncertainties in the soot model (including the lack of aging and aggregate formation effects), by the ability of the chemical kinetic mechanism to predict accurately the concentrations of important species (benzene, propargyl, acetylene and diacetylene) and possibly by the lack of quantitative information concerning the production of translucent particles [18].

Conclusions

A slightly lifted ethylene jet diffusion flame was investigated by comparing results from two sets of experimental diagnostics, one of which was intrusive and the other non-intrusive, and results from a detailed model with fully coupled equations treating radiation and soot formation. The current work is the first to apply a detailed chemistry model with a multiple section soot growth model to a flame that has well represented burner/inlet conditions. Agreement among the experiments and computations is generally good and in some cases excellent. In addition, by comparing the results, we were able to conclude that previously identified discrepancies [5] were likely the result of uncertainties in the burner inlet conditions when the flame is attached to the burner lip. Specifically, uncertain inlet conditions previously led to over prediction of the flame height and high temperatures in the wings of the flame. For the lifted flame, the model was able to reproduce bulk flame parameters extremely well, including flame height, species concentrations, and local temperatures, given some uncertainties in the experiments. The coupled soot model utilized in this and in previous studies reproduced peak soot volume fractions to within 20% but

had some difficulty in reproducing accurately the distribution of soot formed along the centerline of the flame versus that formed along the wings. The formation of benzene as a limit to the inception process was confirmed in this study. Benzene formation was found to be governed by propargyl recombination and propargyl formation, in turn was controlled by reactions involving diacetylene.

Acknowledgments

This work has been supported in part by the Air Force Office of Scientific Research under contract F49620-94-C-0059 and the United States Department of Energy, Office of Basic Energy Sciences. The encouragement of Julian Tishkoff and discussions with R. J. Santoro (Penn State University), R. A. Dobbins (Brown University) and M. A. Tanoff (Yale University) are gratefully acknowledged. The assistance of B. A. Bennett and B. Dobbins (Yale University) was essential in the preparation of the figures.

References

1. Kaplan, C.R., Shaddix, C.R., and Smyth, K.C., *Combust. Flame*, **106**, p.392, (1996).

2. Kennedy, I.M., Rapp, D.R., Santoro, R.J., and Yam, C., *Combust. Flame*, **107**, p.386, (1996).

3. Colket, M.B., and Hall, R.J., in *Soot Formation in Combustion, Mechanisms and Models*, H. Bockhorn, Ed., Springer Series in Chemical Physics **59**, Springer-Verlag, p. 442 (1994).

4. Hall, R.J., Smooke, M.D., and Colket, M.B., in *Physical and Chemical Aspects of Combustion: A Tribute to Irvin Glassman*, ed. by R.F. Sawyer and F.L. Dryer, Combustion Science and Technology Book Series, Gordon and Breach, (1997).

5. Smooke, M. D., McEnally, C. S., Pfefferle, L. D., Hall, R. J. and Colket, M. B., "Computational and Experimental Study of Soot Formation in a Coflow, Laminar Diffusion Flame," submitted to *Comb. and Flame*, (1997).

6. Ern, A., Douglas, C.C., and Smooke, M.D., *Int. J. of Supercomputer Appl.*, **9**, p. 167, (1995).

7. Smooke, M.D., Ern, A., Tanoff, M.A., Valdati, B.A., Mohammed, R.K., Marran, D.F. and Long, M.B., *Twenty-Sixth Symposium (International) on Combustion*, The Combustion Institute, Pittsburgh, 1996, p. 2161.

8. Gelbard, F., and Seinfeld, J.H., *J. Coll. Int. Sci.*, **78**, p. 485. (1980).

9. Harris, S.J., and Weiner, A.M., *Combust. Sci. Tech.*, **31**, p. 155, (1983).

10. Hura, H.S. and Glassman, I., *Twenty-Second Symposium (International) on Combustion*, The Combustion Institute, Pittsburgh, 1988, p. 371.

11. Giovangigli, V. and Darabiha, N., in *Proceedings of the Conference on Mathematical Modeling in Combustion*, Lyon, France, NATO ASI Series (1987).

12. McEnally, C.S., Köylü, Ü.Ö., Pfefferle, L.D., and Rosner, D.E., *Combust. Flame*, **109**, p. 701, (1997).

13. McEnally, C.S., and Pfefferle, L.D., *Combust. Sci. Tech.*, **116-117**, p. 183, (1996).

14. Stårner, S., Bilger, R. W., Dibble, R. W., Barlow, R. S., *Combust. Sci. Tech.*, **86**, p. 223, (1992).

15. Quay, B., Lee, T.-W., Ni, T., and Santoro, R. J., *Comb. and Flame*, **97**, p. 384, (1994).

16. Bowman, C.T., Hanson, R.K., Davidson, D.F., Gardiner, Jr., W.C. Lissianski, V., Smith, G.P., Golden, D.M., Frenklach, M., Wang, H., and Goldenberg, M., *GRI-Mech version 2.11*, http://www.gri.org (1995).

17. Puri, R., Santoro, R. J., and Smyth, K. C., *Combust. Flame*, **97**, p. 125 (1994).

18. Dobbins, R. A. and Fletcher, R. A., *Combust. and Flame*, **100**, p. 301, (1995).

Figure Captions

Figure 1. Schematic of the burner configuration.

Figure 2. Temperature isotherms (K) for the model (left), thermocouple (center) and Rayleigh scattering (right) measurements.

Figure 3. Comparison between the experimental thermocouple temperature measurements and the computed temperatures as a function of the radial coordinate at several axial heights ($\sqcap$=5 mm, o=10 mm, $\diamond$=15 mm, +=20 mm, $\times$=25mm).

Figure 4. Comparison between the computed and experimental benzene mole fraction isopleths.

Figure 5. Comparison of computed (left) and experimental soot volume fraction isopleths. The center picture contains the thermophoretic sampling measurements. The right figure contains the laser-induced incandescence measurements.

Figure 6. Comparison between the computed and experimental (thermophoretic sampling technique) soot volume fraction as a function of the radial coordinate at several axial heights ($\diamond$=18 mm, +=20 mm, $\times$=22mm).

Figure 7. Computed soot surface growth isopleths for the ethylene diffusion flame.

Figure 8. Computed soot inception isopleths for the ethylene diffusion flame.

Figure 9. Computed soot oxidation ($OH + O_2$) isopleths for the ethylene diffusion flame.

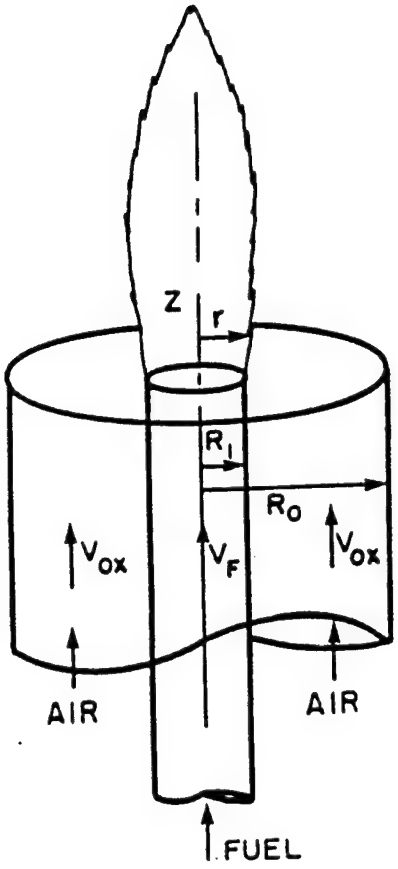

Figure 1

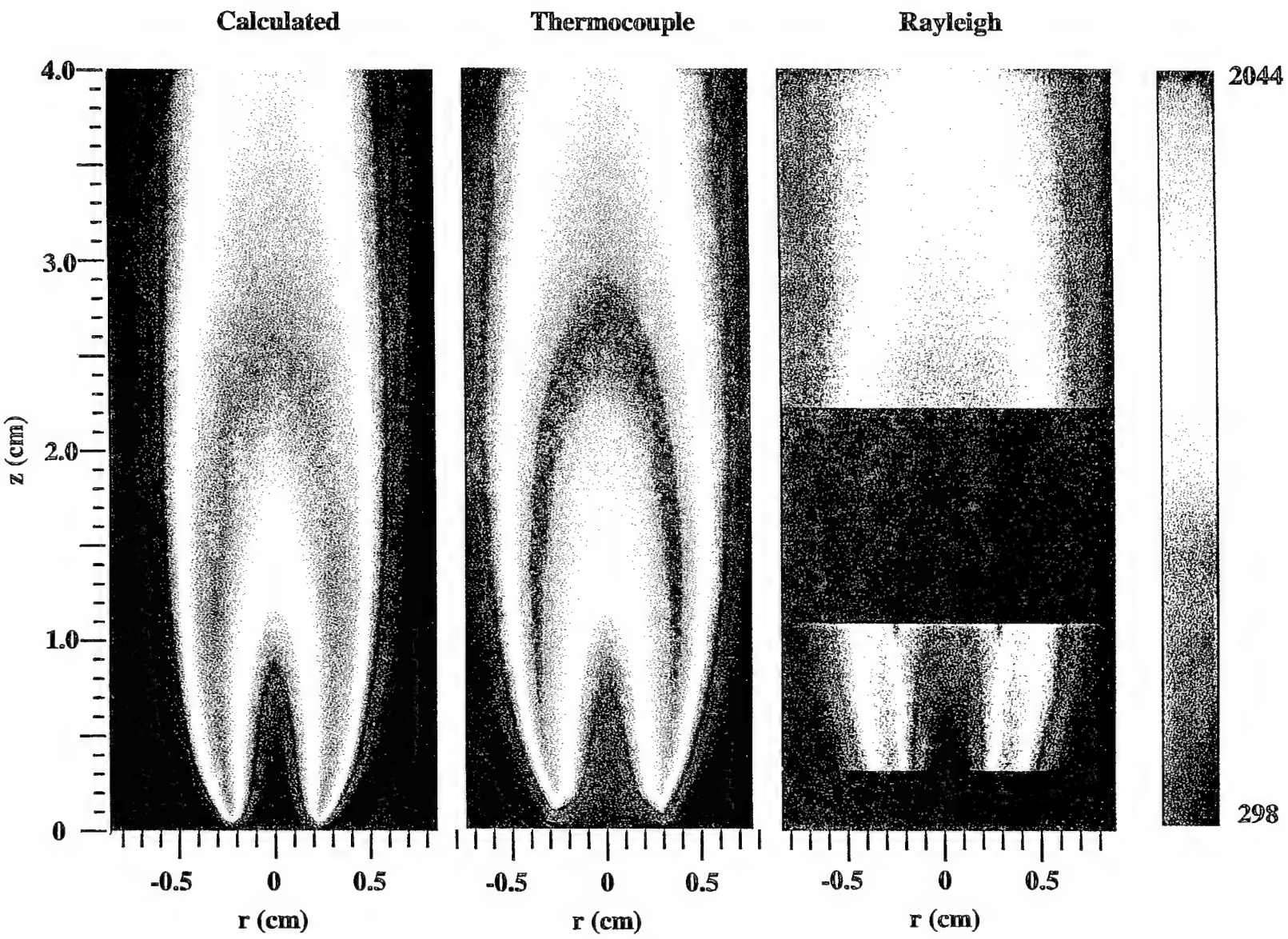
Calculated
Thermocouple
Rayleigh
4.0
3.0
2.0
1.0
0
z (cm)
-0.5
0
0.5
r (cm)
2044
298

Figure 2

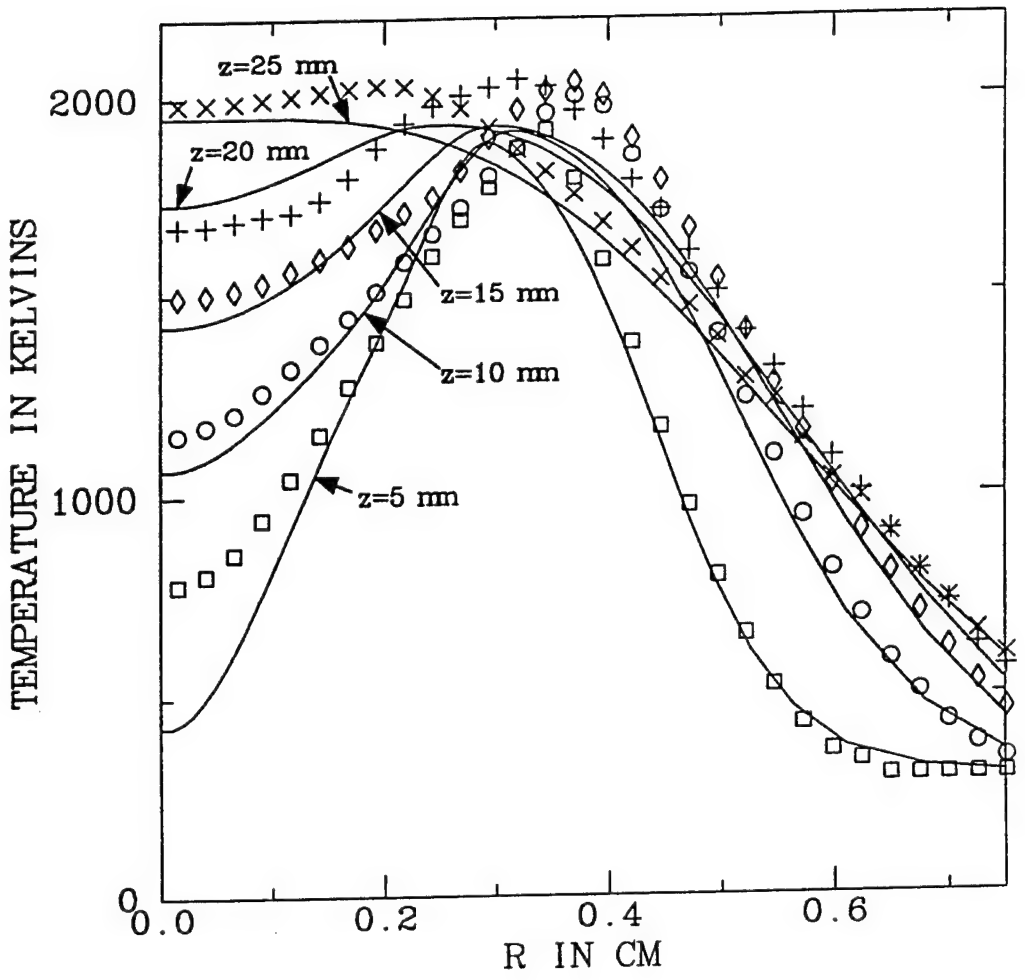
z=25 mm
z=20 mm
z=15 mm
z=10 mm
z=5 mm
2000
1000
0
TEMPERATURE IN KELVINS
0.0
0.2
0.4
0.6
R IN CM

Figure 3

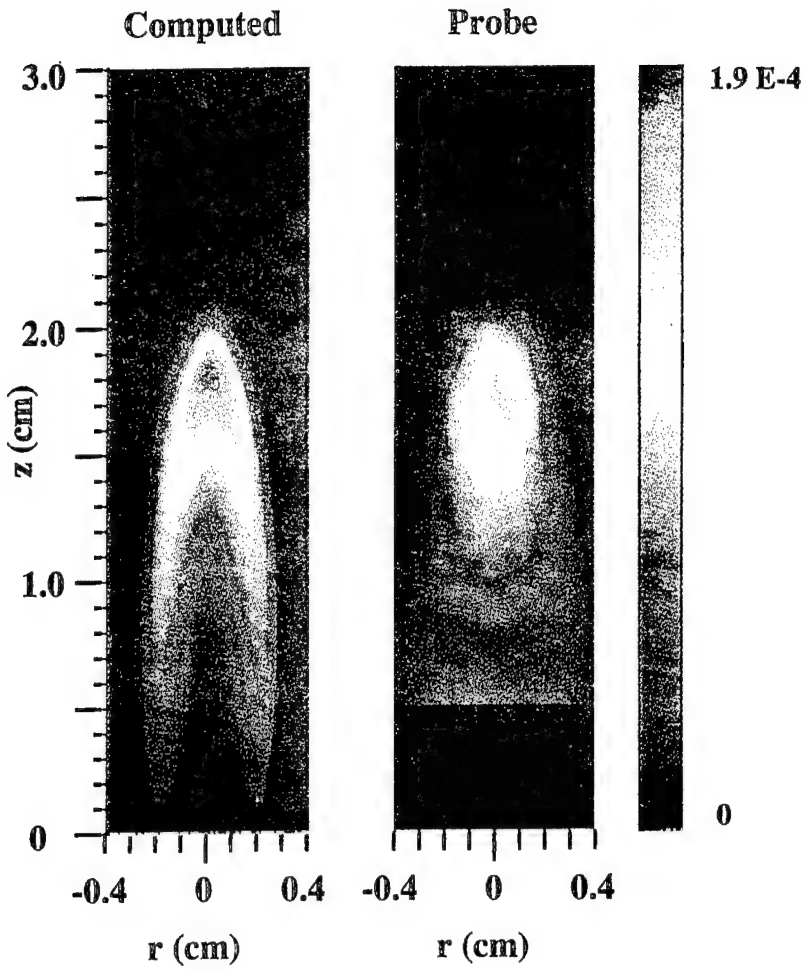

Figure 4

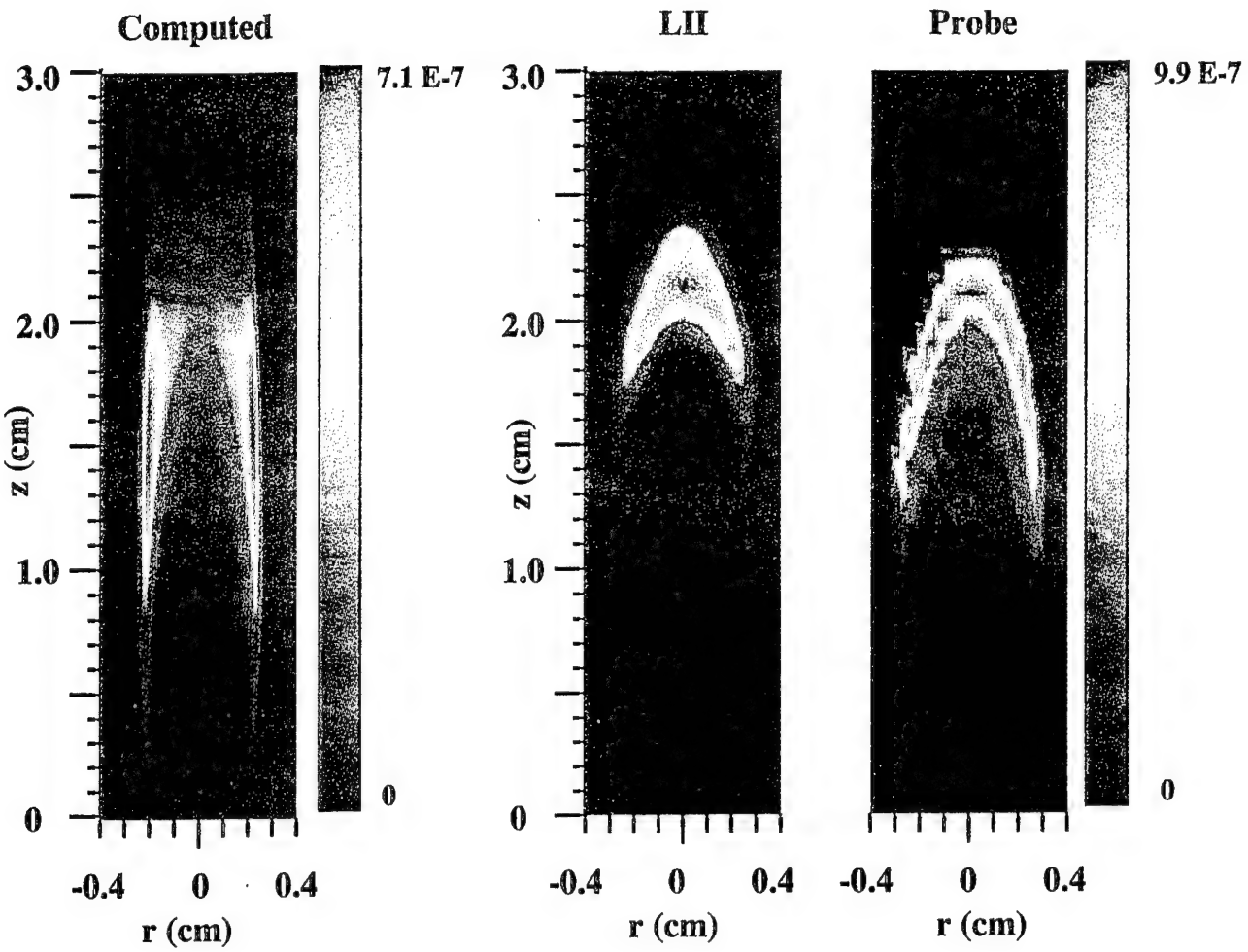

Figure 5

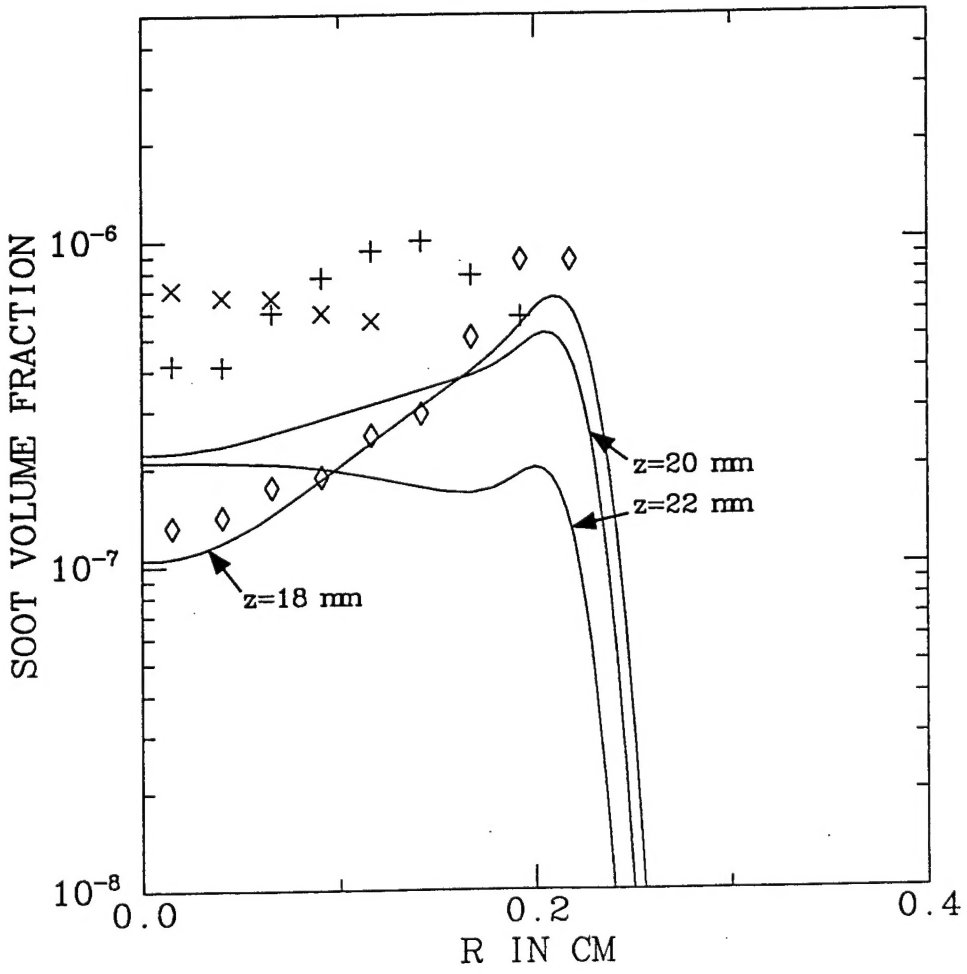
SOOT VOLUME FRACTION
10^{-6}
10^{-7}
10^{-8}
0.0
0.2
0.4
R IN CM
z=20 mm
z=22 mm
z=18 mm

Figure 6

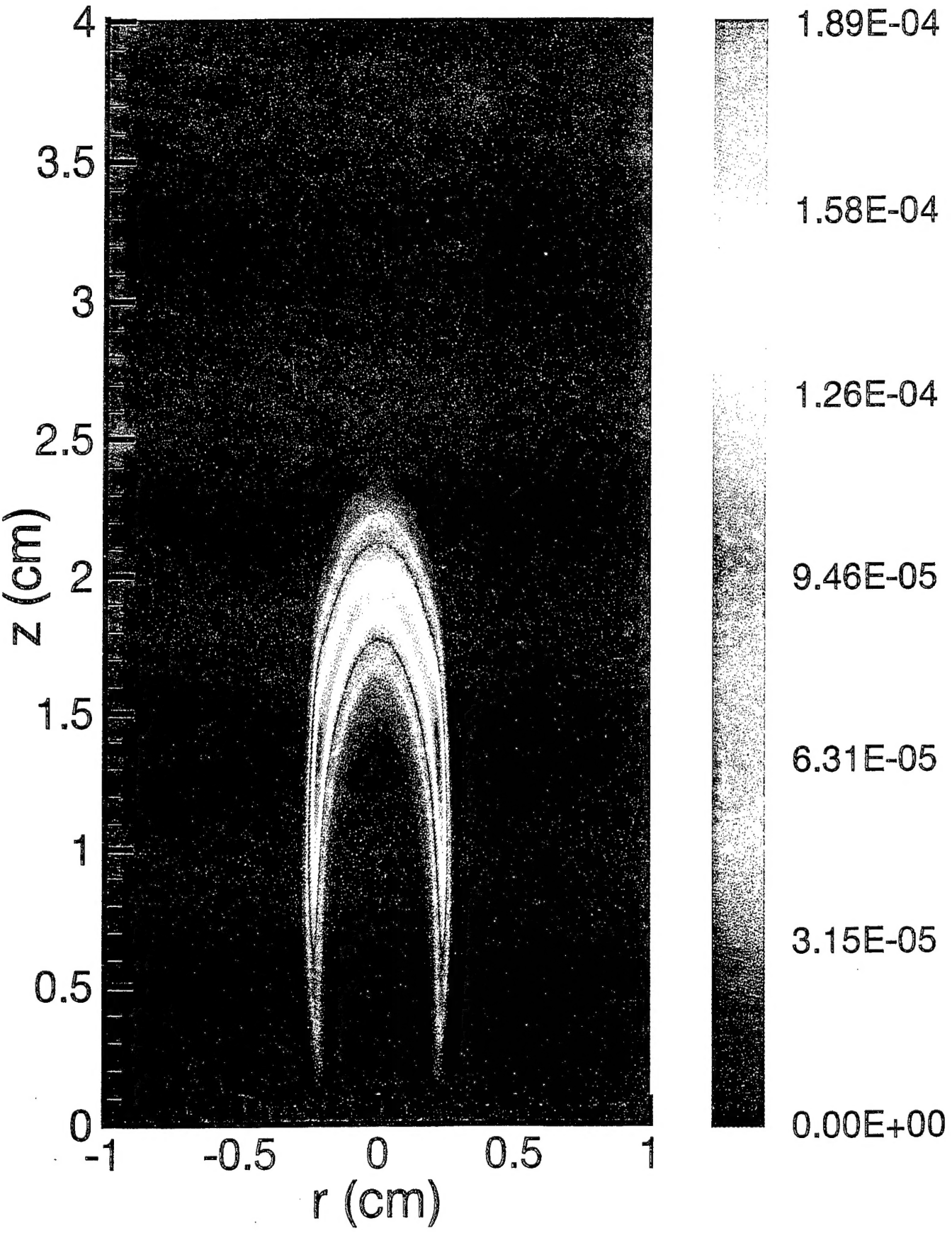
Surface Growth (g/cm3-sec)
1.89E-04
1.58E-04
1.26E-04
9.46E-05
6.31E-05
3.15E-05
0.00E+00
z (cm)
4
3.5
3
2.5
2
1.5
1
0.5
0
-1
-0.5
0
0.5
1
r (cm)

Figure 7

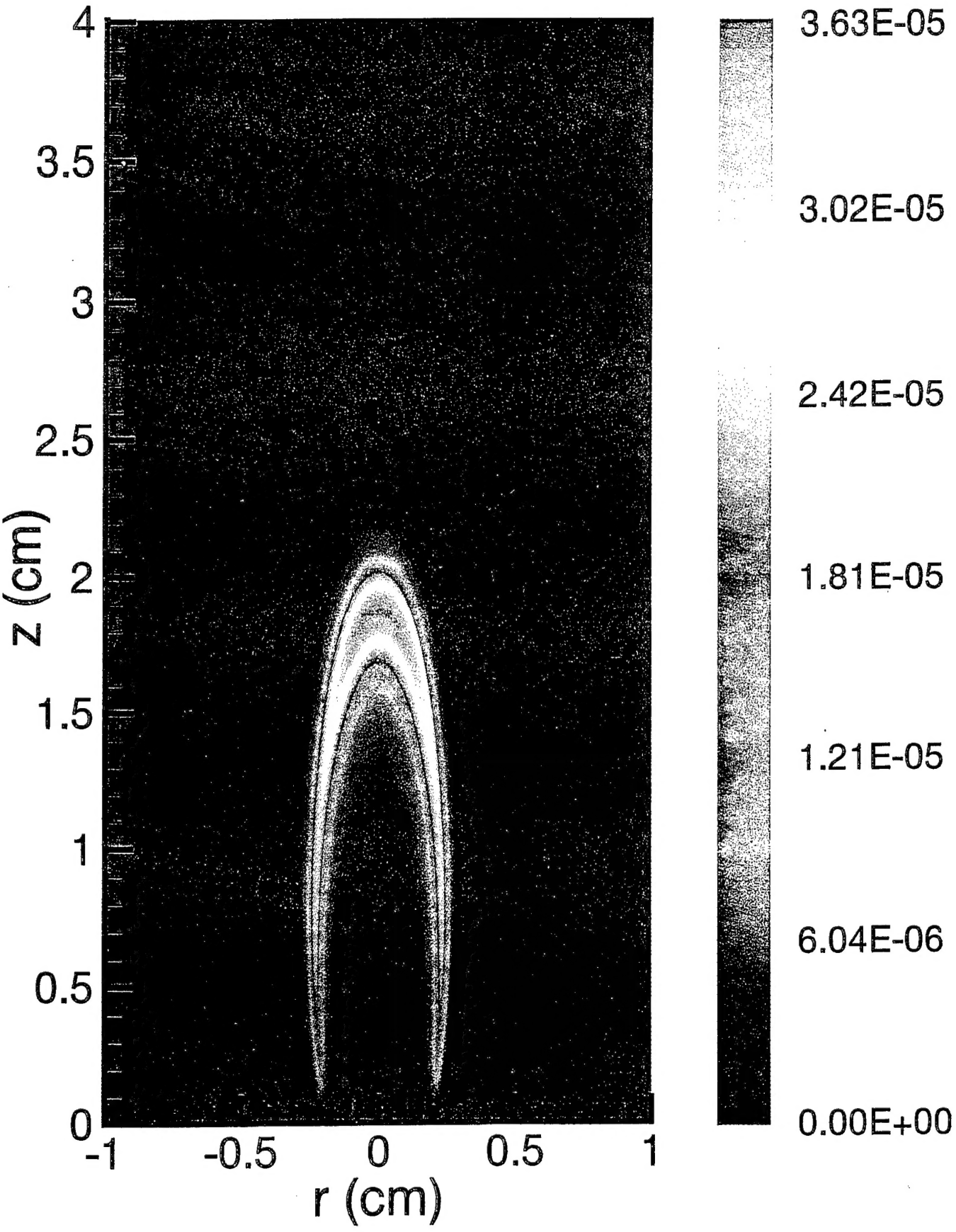
Inception (g/cm3-sec)
4
3.5
3
2.5
2
1.5
1
0.5
0
z (cm)
-1
-0.5
0
0.5
1
r (cm)
3.63E-05
3.02E-05
2.42E-05
1.81E-05
1.21E-05
6.04E-06
0.00E+00

Figure 8

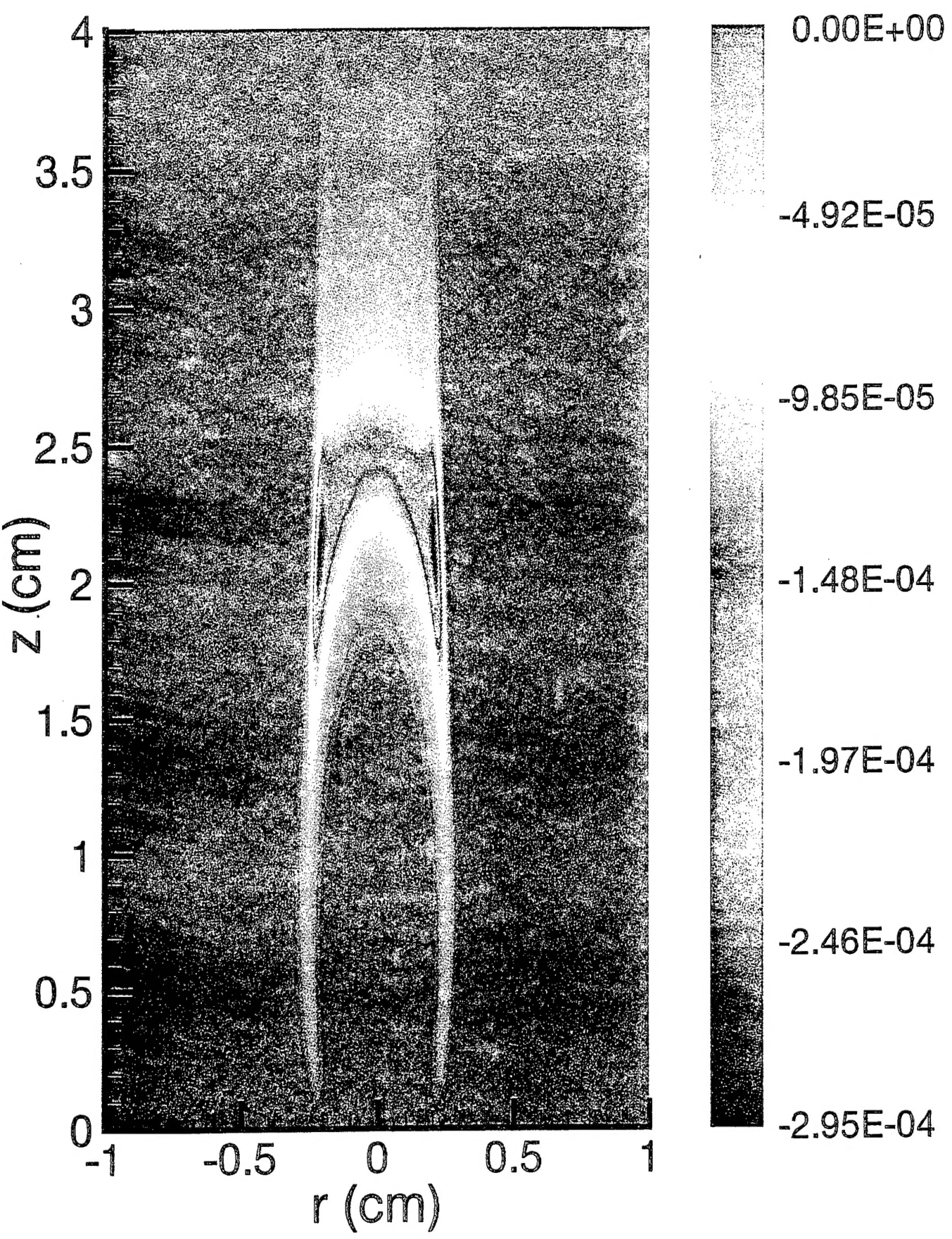
Oxidation (g/cm3-sec)
4
3.5
3
2.5
2
1.5
1
0.5
0
z (cm)
-1
-0.5
0
0.5
1
r (cm)
0.00E+00
-4.92E-05
-9.85E-05
-1.48E-04
-1.97E-04
-2.46E-04
-2.95E-04

Figure 9